J. Fluid Mech. (2006), *vol.* 559, *pp.* 1–44.
doi:10.1017/S0022112005007019 Printed in the United Kingdom

Theory and experiments on the stagnant cap regime in the motion of spherical surfactant-laden bubbles

By RAVICHANDRA PALAPARTHI[1], DEMETRIOS T. PAPAGEORGIOU[2] AND CHARLES MALDARELLI[1]

[1]Levich Institute and Department of Chemical Engineering, City College of New York, Convent Avenue at 140th Street, New York, NY 10031, USA

[2]Department of Mathematical Sciences, and Center for Applied Mathematics and Statistics, New Jersey Institute of Technology, Newark, NJ 07102, USA

(Received 16 July 2002 and in revised form 25 July 2005)

The buoyant motion of a bubble rising through a continuous liquid phase can be retarded by the adsorption onto the bubble surface of surfactant dissolved in the liquid phase. The reason for this retardation is that adsorbed surfactant is swept to the trailing pole of the bubble where it accumulates and lowers the surface tension relative to the front end. The difference in tension creates a Marangoni force which opposes the surface flow, rigidifies the interface and increases the drag coefficient. Surfactant molecules adsorb onto the bubble surface by diffusing from the bulk to the sublayer of liquid adjoining the surface, and kinetically adsorbing from the sublayer onto the surface. The surface surfactant distribution which defines the Marangoni force is determined by the rate of kinetic adsorption and bulk diffusion relative to the rate of surface convection. In the limit in which the rate of either kinetic or diffusive transport of surfactant to the bubble surface is slow relative to surface convection and surface diffusion is also slow, surfactant collects in a stagnant cap at the back end of the bubble while the front end is stress free and mobile. The size of the cap and correspondingly the drag coefficient increases with the bulk concentration of surfactant until the cap covers the entire surface and the drag coefficient is that of a bubble with a completely tangentially immobile surface. Previous theoretical research on the stagnant cap regime has not studied in detail the competing roles of bulk diffusion and kinetic adsorption in determining the size of the stagnant cap angle, and there have been only a few studies which have attempted to quantitatively correlate simulations with measurements.

This paper provides a more complete theoretical study of and a validating set of experiments on the stagnant cap regime. We solve numerically for the cap angle and drag coefficient as a function of the bulk concentration of surfactant for a spherical bubble rising steadily with inertia in a Newtonian fluid, including both bulk diffusion and kinetic adsorption. For the case of diffusion-limited transport (infinite adsorption kinetics), we show clearly that very small bulk concentrations can immobilize the entire surface, and we calculate the critical concentrations which immobilize the surface as a function of the surfactant parameters. We demonstrate that the effect of kinetics is to reduce the cap angle (hence reduce the drag coefficient) for a given bulk concentration of surfactant. We also present experimental results on the drag of a bubble rising in a glycerol–water mixture, as a function of the dissolved concentration of a polyethoxylated non-ionic surfactant whose bulk

diffusion coefficient and a lower bound on the kinetic rate constants have been obtained separately by measuring the reduction in dynamic tension as surfactant adsorbs onto a clean interface. For low concentrations of surfactant, the experiments measure drag coefficients which are intermediate between the drag coefficient of a bubble whose surface is tangentially mobile and one whose surface is completely immobilized. Using the separately obtained value for the diffusion coefficient of the polyethoxylate, we undertake simulations which provide, upon comparison with the measured drag coefficients, a tighter bound on the kinetic rate constants than were otherwise obtained using dynamic surface tension measurement, and this suggests a new method for the measurement of kinetic rate constants.

1. Introduction

The hydrodynamic motion of bubbles and drops moving through a continuous liquid phase can be affected by the presence of surfactants in the system. Initial interest in this subject arose from experimental observations on the terminal velocities of bubbles and drops moving in ostensibly clean liquids by buoyancy. The experiments used fluid particles with diameters small enough so that inertial effects were negligible and the fluid particles translated in straight paths with a near spherical shape. The measured velocities were found to be less then those predicted by the Hadamard–Rybczynski theory for inertialess, rectilinear motion of fluid spheres with a mobile interface; furthermore, as smaller particle diameters were used, the disagreement increased and the velocities approached the Stokes value for a solid sphere (Bond & Newton 1928). A review of the early literature on this phenomenon is given by Clift, Grace & Weber (1978) and recent experiments illustrating this anomalous behaviour are described by Duineveld (1995) and Takemura & Yabe (1999). Levich (Frumkin & Levich 1947; Levich 1962) first provided a consistent explanation for these results by noting that the continuous phase (and the particle phase if the particle is a liquid drop) contained inadvertent trace amounts of surfactant impurities. As the particle translates, surfactant diffuses towards and kinetically adsorbs onto the front end of the bubble and is swept by surface convection to the trailing end where it desorbs and diffuses back into the bulk. At steady state the convective sweeping causes surfactant to accumulate at the back end of the particle making the surface concentration of surfactant at the trailing pole greater than that at the leading pole. As a result of this distribution, the front end of the particle is of higher tension, and tugs at the back end, creating a Marangoni force opposing the surface flow. The resulting reduction in surface mobility decreases the terminal velocity (or alternatively increases the drag coefficient) as the Marangoni force in effect rigidifies the interface.

Experimental research has, in general, verified the Marangoni mechanism by which surfactant affects the fluid particle hydrodynamics, and, in particular, Levich's explanation of the anomalous velocity measurements. This research includes:

(i) Measurements of terminal velocities of bubbles and drops in experiments in which precautions were taken to remove surfactant impurities. The results more closely agreed with either the Hadamard–Rybczynski values or, for experiments using larger particle diameters, the velocity predictions for clean systems including inertial and deformation (cf. the references in Clift *et al.* 1978 and Duineveld 1995). In addition, in the case of bubbles, experiments have used a continuous non-polar phase (rather than water) for which impurities, although not removed, do not adsorb as significantly on

the bubble/non-polar liquid surface (Suzin & Ross 1985; Takemura & Yabe 1999) and achieved excellent agreement with theory.

(ii) Observations of the reduction in the internal circulation of liquid drops, or fluid particle oscillations, at increasing bulk concentrations of surfactant intentionally added to the system. The reduction in circulation and oscillation follows from the reduction in surface mobility (Savic 1953; Garner & Hale 1953; Garner & Skelland 1955; Garner & Haycock 1959; Elzinga & Banchero 1961; Horton, Fritsch & Kintner 1965).

(iii) Measurements of the decrease in interphase mass transfer between the bubble or drop phase and the continuous phase as surfactant is added to the system. This is attributed to the increase in the boundary layer thickness around the fluid particle and the reduction in internal circulation as the interfacial mobility is decreased by the adsorption of surfactant (Garner & Hale 1953; Garner & Skelland 1955; Holm & Terjesen 1955; Lindland & Terjesen 1956; Boye-Christensen & Terjesen 1958; Boye-Christensen & Terjesen 1959; Raymond & Zieminski 1971; Huang & Kintner 1969; Beitel & Heideger 1971; Mekasut, Molinier & Angelino 1978; Skelland, Woo & Ramsay 1987).

(iv) Measurements of the terminal velocities in systems in which surfactants are intentionally added. These invariably show a steady decrease in the terminal velocity with increasing concentration, until a saturating value is achieved. Many of the previously mentioned studies of the reduction in the internal circulation or the decrease in interphase mass transfer observed the reduction in terminal velocity. Other studies in which the measurement of the terminal velocity as a function of surfactant concentration was the primary focus of the study include: Griffith (1962), Edge & Grant (1972), Skelland & Huang (1977), Suzin & Ross (1985), Yamamoto & Ishil (1987), Skelland *et al.* (1987), Bel Fdhila & Duineveld (1996), Sam, Gomez & Finch (1996), Jachimska, Warszynski & Malysa (2001), Zhang & Finch (2001), Zhang, McLaughlin & Finch (2001), Krzan & Malysa (2002), Zhang, Sam & Finch (2003) and Liao *et al.* (2004).

Since Levich's elucidation of the Marangoni mechanism by which surfactant affects the translation of a fluid particle, significant theoretical progress has been made on predicting the velocities of surfactant-laden fluid particles. Viewed in perspective, these studies have shown that the key to predicting the terminal velocity is to understand and formulate the rates of kinetic and bulk diffusive exchange of surfactant from the continuous or drop phase to the surface and the rate of surface diffusion. The ratio of these rates to the rate of surface convection determines the surfactant distribution on the surface which in turn determines the magnitude of the Marangoni force and the retardation in the surface mobility.

The theoretical progress has identified three regimes of surfactant transport which we review here by using scaling arguments for the illustrative case of a bubble with radius a moving with velocity U in a continuous phase with bulk concentration C_0. Consider in more detail the surfactant transport: surfactant adsorbed onto the moving bubble surface is convected by the surface flow from the front of the bubble to its trailing end where the increase in surface concentration, Γ, causes surfactant to kinetically desorb into the rear sublayer. This desorption locally raises the sublayer concentration, C_s, at the back to above the bulk value, C_0, far from the interface. The difference drives a diffusive flux away from the trailing end. Similarly at the front end, the reduction in surface concentration causes kinetic adsorption from the front sublayer onto the front of the bubble. The front sublayer concentration decreases, creating a diffusive flux from the bulk to the front end. Eventually a steady state develops: the surface concentration at the back end has increased by $\Delta\Gamma$ above

the equilibrium value, Γ_o, corresponding to C_0 (as given by the adsorption isotherm $\Gamma_o(C_0)$) so that the desorption rate balances the convective rate. The back sublayer concentration has increased by ΔC above C_0 so that the diffusive flux away from the particle surface balances the kinetic desorption. At the front end, the surface concentration has decreased below Γ_o so that kinetic adsorption balances convection, and the sublayer concentration is reduced below C_0 sufficiently that diffusion to the surface balances adsorption. Thus, while the average concentration on the surface at steady state scales with $\Gamma_o(C_0)$, the surface concentration is considerably higher at the rear than at the front of the particle, and the interfacial tension (γ) is lower at the back than at the front creating the Marangoni force which retards the surface velocity.

We use Langmuir kinetics to scale the kinetic exchange of surfactant between the surface and the sublayer of liquid adjacent to the surface. The kinetic flux of surfactant, j, is given by

$$j = \beta C_s(\Gamma_\infty - \Gamma) - \alpha\Gamma, \tag{1.1}$$

where Γ_∞ is the maximum packing density, α and β are kinetic coefficients for desorption and adsorption, and C_s is the concentration of surfactant adjacent to the interface (i.e. the sublayer concentration). (The Frumkin kinetic scheme, in which rates are proportional to the surface coverage through Arrhenius activation energy terms, have been shown to be more realistic (Chang & Franses 1995), and will be used subsequently in our analysis; however for scaling arguments the Langmuir scheme proves sufficient. For a complete description of kinetic schemes see Borwankar & Wasan 1983.) The average concentration of surfactant on the surface at steady state scales with the equilibrium concentration Γ_o. An expression for the equilibrium concentration is obtained by setting $j = 0$ and noting that the sublayer concentration is the bulk concentration C_0; thus, $\Gamma_o = \Gamma_\infty[k/(1+k)]$ where $k = \beta C_0/\alpha$ is the non-dimensional bulk concentration. Thus a scale for the maximum kinetic rate of adsorption is $\beta\Gamma_\infty C_o$ or equivalently for desorption $(\beta C_o + \alpha)\Gamma_o$. The equilibrium reduction in surface tension for the Langmuir adsorption isotherm is given by $\gamma_c - \gamma_o = \mathscr{R}T\Gamma_\infty \ln(1+k) = -\mathscr{R}T\Gamma_\infty \ln(1-\Gamma_o/\Gamma_\infty)$ (where γ_c and γ_o are the surface tension of the clean interface and the interface with an equilibrium surfactant layer and $\mathscr{R}T$ is the thermal energy). Thus α/β is the surface activity of the surfactant. The smaller this ratio, the more surface active the surfactant is in the sense that lower concentrations give greater reductions in tension. The ratio α/β and the maximum packing concentration are determined from equilibrium measurements of the tension as a function of the bulk concentration; typical values for fairly aqueous soluble surfactants at the air/water interface range from 10^2 mol m^{-3} for the least surface-active alcohols like hexanol to 10^{-6} mol m^{-3} for the very surface-active non-ionic surfactants. Typical values for the maximum packing concentration are 2–6×10^{-6} mol m^{-2} (Chang & Franses 1995). The above description of kinetic exchange is valid for bulk concentrations up to the critical micelle concentration (CMC) (or point of immiscibility of the surfactant). At this concentration, the surface becomes saturated with surfactant and additional surfactant aggregates into micelles in the bulk or forms a separate immiscible phase. In aqueous media, the more surface active the surfactant, the lower the CMC, and thus the maximum value of k is approximately the same and is of order 10^2–10^3. Values for the kinetic rate constants are obtained from measurements of the relaxation in surface tension as surfactant adsorbs onto a clean interface; the kinetic constants are not as well established as the equilibrium

ratio, but values reported for α are in the range of 10^{-4}–$10^{2}\,\mathrm{s}^{-1}$ and values of β follow from the equilibrium ratio (Chang & Franses 1995).

To scale the diffusional transport of surfactant between the bulk and the sublayer, we note that typically convection has a large scale than diffusion in liquids. As an example of a typical system, we can use air bubbles in water and assume a size range for the radii (a) of between 0.1 and 1 mm. Buoyant velocities (U) would then be of the order of 1–40 $\mathrm{cm\,s}^{-1}$ (Clift *et al.* 1978). Diffusion coefficients (D) of surfactants are of the order of $10^{-10}\,\mathrm{m}^2\,\mathrm{s}^{-1}$ (Chang & Franses 1995), and thus the Péclet number Pe (the ratio of convective to diffusive transport) defined as Ua/D varies from 10^4 to 10^6. At these high values of Pe, the diffusion process occurs in a boundary layer close to the surface of the bubble, whose thickness δ, scales as $aPe^{-1/2}$ for a fluid/fluid interface (Acrivos & Goddard 1965). So, δ forms the length scale for the diffusive transport of the surfactant in the bulk liquid. Hence, the scale for the diffusive flux is $D\Delta C/(aPe^{-1/2})$, where ΔC is the characteristic difference between the sublayer and bulk concentration. The maximum diffusive flux to the surface is then $(DC_0)/(aPe^{-1/2})$. The scale for the convective flux is formulated as $(\Gamma_o Ua)/a^2$. Finally the scale for the surface diffusive flux is $D_s\Delta\Gamma/a^2$ where D_s is the surface diffusion coefficient. So the ratio of diffusive to convective flux on the surface is $((\Delta\Gamma)/\Gamma_o)/Pe_s$ where $Pe_s = Ua/D_s$ is the surface Péclet number. As Pe_s is typically large (assuming comparable values for bulk and surface diffusion coefficients), surface diffusion is usually negligible (except in singular cases where large gradients in concentration develop). With the above scales for bulk and surface diffusion, kinetic exchange and surface convection as a reference, three regimes of surfactant transport may be identified as follows:

The stagnant cap regime

In this regime the maximum rate of either the diffusive or kinetic fluxes of surfactant to the surface is much smaller than surface convection. As a result, to leading order, adsorbed surfactant behaves as if it were insoluble, and is swept to the back end of the particle. Using the scales mentioned above, the ratio of the maximum diffusive flux to the surface to the rate of surface convection can be written as $\chi(1+k)/Pe^{1/2}$, where $\chi = \alpha a/(\beta\Gamma_\infty)$. The ratio of the maximum rate of kinetic adsorption to the rate of surface convection can be written as $Bi(1+k)$ where Bi denotes the Biot number and is the desorption rate coefficient divided by the convective rate, $Bi = \alpha a/U$. Thus in the stagnant cap regime we require $\chi(1+k)/Pe^{1/2} \ll 1$ or $Bi(1+k) \ll 1$. If in addition the surface Péclet number is large, then surfactant is swept to a stagnant cap with zero interfacial velocity at the back end since the adsorbed molecules cannot diffuse back to the front. At the front end the surface is clean of surfactant and stress free, as shown in the schematic of figure 1. The size of the stagnant cap is characterized by a cap angle ϕ, measured from the rear stagnation pole.

The stagnant cap regime has been studied by several authors for the case in which inertia is negligible, and the fluid particle is assumed to be a sphere. Savic (1953), Griffith (1962), Harper (1973) (for small cap angles), Davis & Acrivos (1966), Holbrook & Levan (1983*b*), Sadhal & Johnson (1982), and He, Maldarelli & Dagan (1991) all solved the creeping flow equations to obtain the drag as a function of the cap angle for the buoyancy-driven motion of spheres. Kim & Subramanian (1989) studied the analogous problem of stagnant caps formed in the thermocapillary-driven motion of spheres. Bel Fdhila & Duineveld (1996), McLaughlin (1996), and Zhang *et al.* (2001) extended these studies to buoyancy-driven bubble flows in water in which the fluid inertia is not negligible (order-one Reynolds number (Re), where

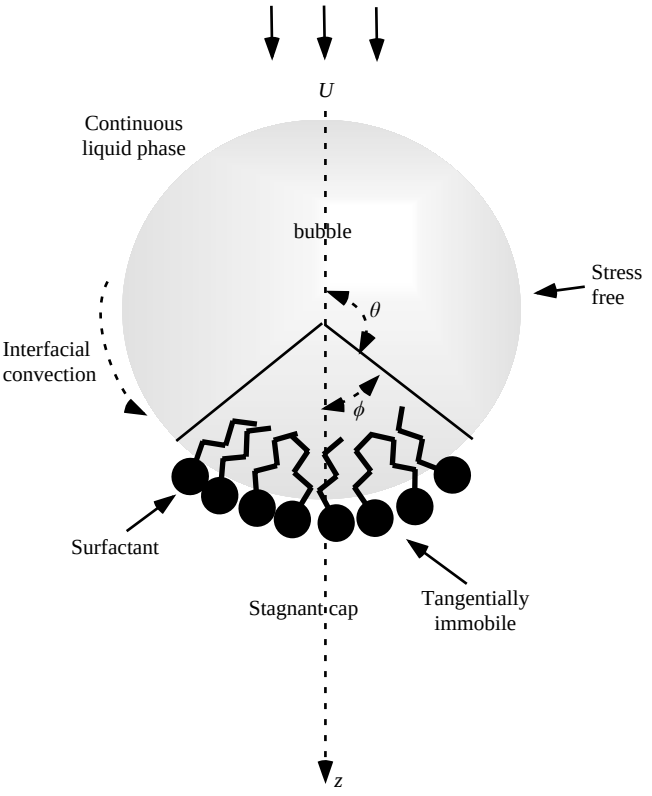

FIGURE 1. Stagnant cap model for the surfactant distribution on the surface of a translating bubble.

$Re = Ua\rho/\mu$, ρ and μ being respectively the density and Newtonian viscosity of the continuous phase) and demonstrated the formation of a wake at the trailing edge due to the stagnant cap.

The calculation of the drag coefficient as a function of the cap angle is a fluid mechanical problem and the cap angle itself is treated as a variable in the calculation. The value of the cap angle is determined by the solution of the surfactant transport and is a function of the bulk concentration of surfactant or k. This relationship ($\phi(k)$) is obtained by solving the surfactant transport equations and requiring that the net flux of surfactant to the surface equals zero at steady state (Harper 1973; He *et al.* 1991). The relationship ($\phi(k)$) together with the drag as a function of the cap angle provides a complete description of the immobilization, and in particular answers the question of how much surfactant has to be dissolved in the system to immobilize the surface completely. For kinetic control (He *et al.* 1991; McLaughlin 1996; Bel Fdhila & Duineveld 1996) studies have shown that the cap angle increases quickly with bulk concentration k from a clean to a fully covered and completely tangentially immobile surface.

More complete studies taking into account finite rates of both kinetic exchange and diffusive transport of the surfactant have been undertaken by Cuenot, Magnaudet & Spennato (1997), Liao & McLaughlin (2000*a*), Liao *et al.* (2004) and Takemura (2005). These studies solved the convection diffusion equation along with the hydrodynamic equations for order-one Re without the *a priori* assumption of a stagnant cap, but for conditions in which a cap would be formed by both kinetic and bulk diffusive restrictions. They demonstrated that the surfactant does organize itself into a stagnant

cap at the trailing end of the bubble. The cap angle and terminal velocity (or alternatively drag) were calculated for values of k corresponding to intermediate cap angles, although no systematic study of the functional dependence was undertaken. Analytical expressions for mixed control in the stagnant cap regime using a boundary layer analysis have been obtained by Harper (2004) and the stagnant cap regime has also been studied in the context of its effect on the dissolution of translating bubbles composed of gases soluble in the continuous phase (see, among others, Takemura & Yabe 1999; Ponoth & McLaughlin 2000; Liao & McLaughlin 2000*b*).

Uniformly retarded regime

When the rates of bulk diffusion and surfactant kinetic exchange are of the same order as the interfacial convection, surfactant exchanges between the bulk and the surface. Within the framework of the scales developed above, the uniformly retarded regime is realized when $Bi(1+k) = O(1)$ and $\chi(1+k)/Pe^{1/2} = O(1)$. In this case, the surface of the bubble becomes more uniformly retarded rather than, as the case with the stagnant cap, completely mobile at the front end and solid-like at the back. In particular, the balancing of the diffusive rate with the convective rate provides a scale for the difference between the bulk and sublayer concentrations ΔC:

$$\frac{a^2 D \Delta C}{a Pe^{-1/2}} = O(\Gamma_o U a)$$

or

$$\frac{\Delta C}{C_0} = O\left(\frac{Pe^{1/2}}{\chi(1+k)}\right).$$

The balancing of the kinetic rate to the convective rate provides a scale for $\Delta\Gamma$:

$$Bi(1+k)\left(\frac{\Delta C}{(1+k)C_0} - \frac{\Delta\Gamma}{\Gamma_o}\right) = O(1).$$

In the creeping flow limit, this case has been studied by several authors at low surfactant concentrations ($k < 1$) for both kinetic and diffusion-limited transport (Deryagin, Dukhin & Lisichenko 1959, 1960; Levich 1962; Dukhin & Buikov 1965; Harper 1972; 1974; Levan & Newman 1976; Harper 1982; Holbrook & Levan 1983*a*; Saville 1973; Andrews, Fike & Wong 1988; Harper 1988; Leppinen, Renksizbulut & Haywood (1996*a*, *b*) and order-one values of k for kinetically limited transport (Chen & Stebe 1996, 1997; Ybert & Meglio 2000).

Remobilization regime

In the limit in which the bulk concentration is large $k \gg 1$ and the kinetic and bulk diffusive exchange are fast relative to convection ($\chi(1+k)/Pe^{1/2} \gg 1$ and $Bi(1+k) \gg 1$) the difference between the bulk and sublayer concentrations becomes small relative to C_0,

$$\frac{\Delta C}{C_0} = \frac{Pe^{1/2}}{\chi(1+k)} \ll 1.$$

Since the kinetic rate is much faster than the convective rate, the surface and sublayer are in equilibrium so that the variation in the surface concentration from the equilibrium $\Delta\Gamma$ is small and can be related to the small variation in ΔC:

$$\frac{\Delta\Gamma}{\Gamma_\infty} = \frac{kPe^{1/2}}{\chi(1+k)^3}.$$

This latter quantity tends to zero (as k becomes large) indicating that the surface concentration becomes uniform, and the Marangoni force disappears. This regime

has been investigated for the case of diffusion-limited transport of the surfactant (i.e. $Bi \to \infty$, and $\chi(1+k)/Pe^{1/2} = O(1)$), by Wang, Papageorgiou & Maldarelli (1999) for small Re, and for order-one Re by Wang, Papageorgiou & Maldarelli (2001) and Takemura (2005).

For the typical system we have considered of air bubbles 0.1–1 mm in radius rising in water with velocities 1–40 cm s^{-1}, it is easy to see that the regime which is most commonly realized is the stagnant cap regime. The surface Péclet number, as we mentioned above, is typically very large for these conditions. The parameter $\chi/a = \alpha(\Gamma_\infty \beta)$, which is only a function of the surfactant chemistry, is strongly dependent on the surfactant activity. From the values discussed above, this parameter ranges between 1 m^{-1} (for the most surface-active surfactants) and 10^8 m^{-1} for the least surface-active surfactants (see Chang & Franses 1995). The parameter χ is therefore between 10^5 (for the largest radii and-least surface-active surfactants) and 10^{-4} (for the smaller radii and most surface-active surfactants). Thus at low or trace concentrations of a very surface-active surfactant, i.e. $k \ll 1$, or even $k = O(1)$, $\chi(1+k)/Pe^{1/2} \ll 1$ and bulk diffusion limitations alone can result in the stagnant cap limit (recall that Pe varies between 10^4 and 10^6). These arguments show in particular why very surface-active materials in trace amounts ($k \ll 1$) lead to the stagnant cap regime, and uniform retardation and remobilization are only realized at higher concentrations ($k \gg 1$) of less surface-active surfactants. (As we mentioned above, values for k can range up to 10^3 before the critical micelle concentration is reached.) With regard to kinetic limitations, kinetic rate constants are not well established. Values for α are in the range of 10^{-4}–10^2 s^{-1}, depending on the surfactant (Chang & Franses 1995). Thus, kinetic limitations can also give rise to the insoluble limit since Bi ranges from 10^{-6} to 1.

While the stagnant regime is the usual one realized in the typical case of fluid particles buoyantly moving in an aqueous system containing a surface-active impurity, and, furthermore, has been the regime most extensively studied theoretically, few comparisons have been made between measurements of terminal velocities in the stagnant cap regime and theoretical computations. The early experimental evidence on the reduction in circulation inside drops by Savic (1953) and Horton *et al.* (1965) among others also showed the shift in the centre of the circulation vortex to the leading edge, reflecting that a stagnant cap had formed on the surface of the drop. Aside from these qualitative observations, the first attempt at a quantitative comparison between stagnant cap theory and experiment was Griffith's (1962) study of the motion of droplets with surfactant added to the system. Griffith interpreted his results in terms of the stagnant cap model, but the calculation of the cap angle as a function of the bulk concentration by solution of the surfactant transport equations was not undertaken. Bel Fdhila & Duineveld (1996) performed experiments measuring the reduction in the terminal rise velocity of air bubbles in water as a function of increasing bulk concentration of a dissolved non-ionic surfactant, Triton X-100. These authors verified from the scaling arguments that the bubbles were moving in the stagnant cap regime, and compared the experimental results to stagnant cap theoretical calculations which solved the surfactant transport equations but assumed (as we mentioned above) only a kinetic limitation to the surfactant transfer. The simulations showed qualitative agreement with the experiments, in part due to the fact that the effects of bulk diffusion were not included. The discrepancy may also be attributed to the fact that the velocities may not have achieved their terminal values, as pointed out by Zhang & Finch (2001) (see also Zhang *et al.* 2001). These authors performed their own experiments for air bubbles in Triton X-100 solutions carefully ensuring that a terminal velocity had been reached. They demonstrated

that the terminal velocity for the concentration range they used was independent of concentration, and close to the value expected for a rigid particle. The decrease in terminal velocity with bulk concentration as predicted by theory was not observed, perhaps because the concentrations in the range used were already too large and the rigid interface had already been achieved.

The objective of this paper is to obtain a quantitative agreement between experiments and theory for surfactant-laden spherical bubbles rising in liquids in the stagnant cap regime. Our first objective is to present complete solutions for the stagnant cap angle and drag as a function of bulk concentration of surfactant including both kinetic and bulk diffusion limitations. We will also compare the results of Langmuir adsorption, which is the only model which has been used in stagnant cap modelling, and the more realistic Frumkin adsorption which includes molecular interactions in the adsorbed monolayer. Our second objective is to undertake experiments measuring the terminal velocity of bubbles at increasing bulk concentrations of a surfactant, to demonstrate a reduction in the velocity with concentration from the clean-interface value to that for a rigid particle, and to compare simulations using measured surfactant parameters to the velocity measurements. The experiments are undertaken in a glycerol–water continuous phase with a viscosity approximately thirty times that of water and with bubbles of approximately 0.3–0.8 mm in radius. Under these conditions the velocity of bubbles of this size is reduced sufficiently compared to that of water that the bubbles translate rectilinearly and inertia does not distort the bubbles from spherical shapes. Reynolds numbers are still of order one. We use a polyethylene oxide surfactant $C_{12}E_6(CH_3(CH_2)_{11}(OCH_2CH_2)_6OH)$ for the surface-active agent, and its equilibrium and kinetic parameters and diffusion coefficient are measured separately by dynamic tension measurements.

An outline of this paper is as follows. In § 2 we formulate the mathematical model; our numerical algorithms for solving the governing equations for the stagnant cap hydrodynamics and surfactant transport, accounting for finite rates of transport of the surfactant by diffusion-in the bulk and kinetic exchange at the interface, are detailed in the Appendix. In § 3 we present and discuss the results of our simulations. In § 4 we describe our experiments on measuring the drag coefficient on a gas bubble rising in a glycerol–water mixture containing ($C_{12}E_6$), and compare the simulations with the experiments. Section 5 contains concluding remarks.

2. The mathematical model

Consider a spherical bubble of radius a, moving steadily and axisymmetrically (in the negative z-direction) with velocity U due to buoyancy in a continuous phase containing surfactant. We undertake the analysis in a spherical coordinate system fixed to the bubble with the centre of the spherical system at the bubble centre and the spherical angle θ taken from the negative z-direction as shown in figure 2. In this moving reference system, the bubble interface is fixed, and the flow far from the bubble is in the positive z-direction. The viscosity and density of the continuous phase are denoted by μ and ρ respectively, and γ_c is the value of the surface tension for a clean interface. The continuous phase contains surfactant with a bulk concentration (far from the bubble surface) equal to C_0. The assumption of the bubble being spherical is valid if both the inertial and viscous forces are small compared to surface tension forces (i.e. the Weber number, $We = \rho U^2 a/\gamma_c$, and the capillary number, $Ca = \mu U/\gamma_c$, are small). The flow around the bubble is described by the incompressible Navier–Stokes equations coupled to a surfactant transport equation. In non-dimensional form

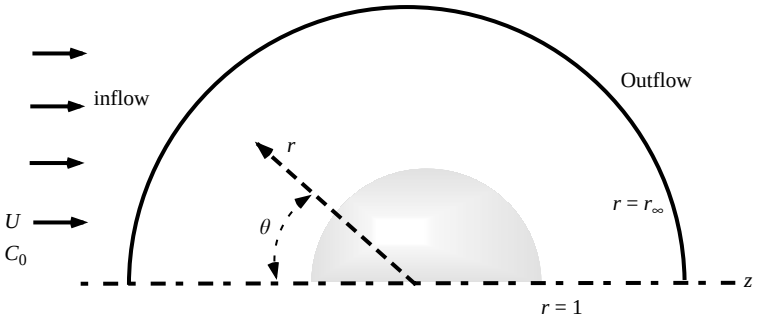

FIGURE 2. Definition sketch of the computational domain which is restricted from the bubble surface $r=1$ to infinity $r=r_\infty$. A value of 80 bubble radii is chosen for r_∞. The outer boundary is divided into inflow and outflow regions at $\theta=\pi/2$.

these equations are

$$Re[\boldsymbol{v}_t + \boldsymbol{v}\cdot\nabla\boldsymbol{v}] = -\nabla P + \nabla^2\boldsymbol{v}, \tag{2.1}$$

$$\nabla\cdot\boldsymbol{v} = 0, \tag{2.2}$$

$$C_t + \boldsymbol{v}\cdot\nabla C = \frac{1}{Pe}\nabla^2 C. \tag{2.3}$$

In arriving at (2.1)–(2.3), lengths, velocities, surfactant concentration C, and pressure P are non-dimensionalized with the bubble radius a, the free-stream velocity U, bulk concentration C_0, and $\mu U/a$, respectively; in what follows u and v denote radial and azimuthal components of the velocity vector $\boldsymbol{v}$; the Reynolds and Péclet numbers are given by $Re=Ua\rho/\mu$ and $Pe=Ua/D$, respectively, with D being the diffusion coefficient of the surfactant in the liquid. Although we are interested in steady-state solutions, we-formulate and work with the unsteady problem for numerical purposes (see below).

At the surface of the spherical bubble, the radial component of velocity is equal to zero. The presence of surfactant creates a surface tension gradient and causes a force on the bubble surface that must be compensated by a viscous tangential stress on the interface. In dimensionless form this is

$$\frac{\partial\gamma}{\partial\theta} = \frac{\partial\gamma}{\partial\Gamma}\frac{\partial\Gamma}{\partial\theta} = -Ca\tau_{r\theta} \quad \text{on} \quad r=1, \tag{2.4}$$

where $\tau_{r\theta}$ is the dimensionless shear stress, Γ is the dimensionless surface concentration non-dimensionalized by the maximum packing concentration Γ_∞, and γ is the dimensionless surface tension non-dimensionalized by the clean value γ_c. To model the surfactant adsorption, Frumkin kinetics will be used since this scheme describes accurately the kinetics of a wide range of surfactants. The equation of state for this kinetic scheme is given by (see Chang & Franses 1995)

$$\gamma = 1 + MaCa\left[\ln(1-\Gamma) - \frac{K}{2}\Gamma^2\right], \tag{2.5}$$

from which the boundary condition (2.4) on the surface of the bubble becomes

$$[\tau_{r\theta}]_{r=1} = \left[r\frac{\partial}{\partial r}\left(\frac{v}{r}\right)\right]_{r=1} = Ma\left[\frac{1}{1-\Gamma} + K\Gamma\right]\frac{\partial\Gamma}{\partial\theta}, \tag{2.6}$$

where $Ma=\mathscr{R}T\Gamma_\infty/\mu U$ is the Marangoni number, $\mathscr{R}$ is the gas constant, T is the temperature, and K is a parameter accounting for intermolecular interactions among

the molecules of the adsorbed layer at increasing surface concentration ($K=0$ gives the Langmuir type kinetics; K larger than 0 are repulsive interactions and K less than zero are attractive interactions). The Marangoni number is a measure of the forces due to surface tension gradients relative to the viscous forces.

The surfactant distribution on the bubble is computed from a surface mass balance. Surfactant transport into the air interior of the bubble is neglected. Under these conditions, the balance equation for the interfacial concentration, and with kinetics described by the Frumkin scheme, can be written as (see Edwards, Brenner & Wasan 1991)

$$\Gamma_t + \frac{1}{\sin\theta}\frac{\partial}{\partial\theta}(\sin\theta\,\Gamma v_s) = \frac{1}{Pe_s}\frac{1}{\sin\theta}\frac{\partial}{\partial\theta}(\sin\theta\,\Gamma_\theta) + Bi(kC|_{r=1}(1-\Gamma) - \mathrm{e}^{K\Gamma}\Gamma), \quad (2.7)$$

$$Bi(kC|_{r=1}(1-\Gamma) - \mathrm{e}^{K\Gamma}\Gamma) = \frac{\chi k}{Pe}C_r|_{r=1}. \quad (2.8)$$

Here Γ is the non-dimensional surface concentration, v_s is the azimuthal component of the velocity $\boldsymbol{v}$ on the surface of the bubble, $k=\beta C_0/\alpha$ is a measure of bulk concentration (α and β are the (Frumkin) desorption and adsorption rate constants respectively), and $Bi=\alpha a/U$, the Biot number, is the ratio of the rate of kinetic desorptive exchange of the surfactant at the gas/liquid interface to the rate at which it is convected from the front end to the rear end due to the bulk flow. At infinity the boundary conditions for the flow and concentration match their free-stream values:

$$\boldsymbol{v} = u\boldsymbol{e}_r + v\boldsymbol{e}_\theta \text{ i.e. } u = -\cos\theta,\ v = \sin\theta \text{ as } r\to\infty, \quad (2.9)$$

$$C(r,\theta)\to 1 \text{ as } r\to\infty. \quad (2.10)$$

Finally, we note that the drag coeffcient on the bubble is given by

$$C_D = \int_0^\pi (-P\cos\theta + \tau_{rr}\cos\theta - \tau_{r\theta}\sin\theta)_{r=1}\sin\theta\,\mathrm{d}\theta, \quad (2.11)$$

where $\tau_{rr}=2\partial u/\partial r$. Here the drag is non-dimensionalized by the viscous force $2\pi\mu Ua$. Using these scalings, the values of C_D in the creeping flow limit are 2 for flow past a spherical bubble and 3 for flow past a solid sphere.

As explained in the Introduction, in the limits in which $Pe_s \gg 1$ and either the kinetic or diffusive rates of surfactant adsorption are much smaller than surface convection, a stagnant cap is formed at the trailing pole of the bubble. The scaling arguments which define these regimes are discussed in the Introduction for the case of Langmuir adsorption. For Frumkin adsorption, the equilibrium surface concentration used in the scaling is given by $\Gamma_o/\Gamma_\infty = k/(k+\mathrm{e}^{K\Gamma_o/\Gamma_\infty})$ and the defining criterion for the stagnant cap regime becomes with these kinetics: $Bi(\mathrm{e}^{K\Gamma_0/\Gamma_\infty}+k) \ll 1$ or $\chi(\mathrm{e}^{K\Gamma_0/\Gamma_\infty}+k)/Pe^{1/2} \ll 1$.

In the stagnant cap limit, in the balance equation (2.7) for Γ, the advective term vanishes when steady-state conditions are reached, see Savic (1953). Then (2.7) in conjunction with (2.8) reduces to

$$\frac{1}{\sin\theta}\frac{\partial}{\partial\theta}(\Gamma v_s\sin\theta) = 0. \quad (2.12)$$

Applying the boundary conditions of zero fluxes at the stagnation points then leads to

$$\Gamma v_s = 0. \quad (2.13)$$

This shows that the interface contains essentially two different regions. Between the front stagnation point and the beginning of the cap, the interface is free of surfactant. Thus according to the equation (2.4), this part is subjected to a stress-free boundary

condition, that is,

$$0 < \theta < \pi - \phi \begin{cases} v(r=1,\theta) \neq 0, \\ \tau_{r\theta}(r=1,\theta) = 0, \\ \Gamma(\theta) = 0, \end{cases} \tag{2.14}$$

In this stress-free region equation (2.8) becomes

$$BiC|_{r=1} = \frac{\chi}{Pe} C_r|_{r=1}. \tag{2.15}$$

On the stagnant cap at the back end of the bubble, the condition (2.13) predicts a zero surface velocity, namely,

$$\pi - \phi < \theta < \pi \quad \begin{cases} v(r=1,\theta) = 0, \\ \tau_{r\theta}(r=1,\theta) = \tau_s(\theta;\phi) \neq 0, \\ \Gamma(\theta) \neq 0, \end{cases} \tag{2.16}$$

The non-zero surface concentration at the back end is obtained by integration of the Marangoni stress condition (2.6) to give

$$\frac{1}{2} K \Gamma(\theta)^2 - \ln(1 - \Gamma(\theta)) = \frac{1}{Ma} \int_{\pi-\phi}^{\theta} \left[\frac{\partial v}{\partial r} - v \right]_{r=1} \mathrm{d}\theta. \tag{2.17}$$

The matching of the diffusive flux to the kinetic exchange, see (2.8), provides the boundary condition for the concentration in this region with $\Gamma(\theta)$ given above, that is

$$\frac{\chi}{BiPe} \frac{\partial C}{\partial r}(1,\theta) = C(1,\theta)[1 - \Gamma(\theta)] - \frac{1}{k} \Gamma(\theta) \exp(K\Gamma(\theta)), \quad \pi - \phi < \theta < \pi. \tag{2.18}$$

Given a cap angle ϕ, then the above velocity and concentration boundary conditions should be used to solve the Navier–Stokes equations and the convection–diffusion equation for C, to determine solutions. Note that with ϕ arbitrarily prescribed, these stagnant cap equations are well-posed and a steady solution follows. The integral of the steady version of (2.7) along with (2.8) establishes that the net transport of surfactant onto the surface, which defines a non-dimensional Nusselt number Nu, is equal to zero, that is,

$$Nu = \int_0^{\pi} \left[\frac{\partial C}{\partial r} \right]_{r=1} \sin\theta \, \mathrm{d}\theta = 0. \tag{2.19}$$

Note that this constraint is independent of the values of Bi and Pe and is therefore valid even in the stagnant cap limit where Bi is small and Pe is large. In the stagnant cap regime, this final condition (2.19) determines the cap angle and hence the flow and concentration fields.

3. Numerical results

The Appendix describes the numerical solution procedures for solving the stagnant cap hydrodynamic and surfactant mass transfer equations which were detailed in the previous section. Here we present numerical results, focusing particularly on the dependence of the cap angle and drag coefficient as a function of the bulk concentration of surfactant. The values of the non-dimensional groups used in the simulations correspond to the conditions of the experiments where air bubbles rise in glycerol/water solutions of the polyethoxylate surfactant $C_{12}E_6$. For this surfactant, as we discuss in the Experimental Section (§4), equilibrium and dynamic tension

CMC, mol m^{-3}	0.209
Γ_∞, mol m^{-2}	4.48×10^{-6}
K	5.47
D, m^2 s^{-1}	1.5×10^{-11}
α/β, mol m^{-3}	9×10^{-4}
β, m^3 mol^{-1} s^{-1}	>10
α, s^{-1}	$>9 \times 10^{-3}$
Re	0.91
Ma	12.6
Pe	1.2×10^6
χ	0.12
Bi_{min}	1.55×10^{-4}

TABLE 1. Properties of $C_{12}E_6$ in 70:30 glycerol–water mixture and characteristic values of non-dimensional groups.

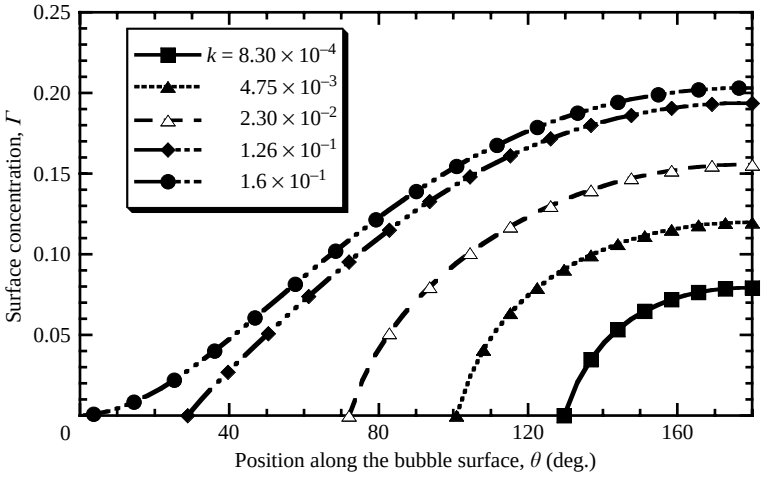

FIGURE 3. Surfactant surface concentration as a function of angle for different bulk concentrations k for a diffusion-limited case and Langmuir adsorption for parameter values as given in table 1.

experiments (for adsorption onto an initially clean interface) were undertaken to obtain the critical micelle concentration, the Frumkin adsorption parameters K, α, β, and Γ_∞ and the diffusion coefficient D. These are summarized in table 1, where we note that only a lower bound could be established for the kinetic rate constants due to the fact that the high viscosity of the solution reduces the diffusion coefficient and makes the diffusion process rate limiting. Using these parameters, and from the experimental measurements characteristic values for the viscosity and density of the glycerol/water mixture, the rise velocity U and the bubble radius a, we compute representative values of Re, Ma, Pe, χ, and a lower bound for the Biot number Bi_{min}. These, as detailed in table 1, are used in the simulations.

3.1. *Diffusion-limited transport and Langmuir adsorption*

Consider first the case of diffusion-limited transport ($Bi \to \infty$) when the surfactant follows Langmuir type kinetics (i.e. when $K = 0$ in equation (2.5)); the values of Re, Ma, Pe and χ are those given in table 1. In figure 3 we plot the surfactant

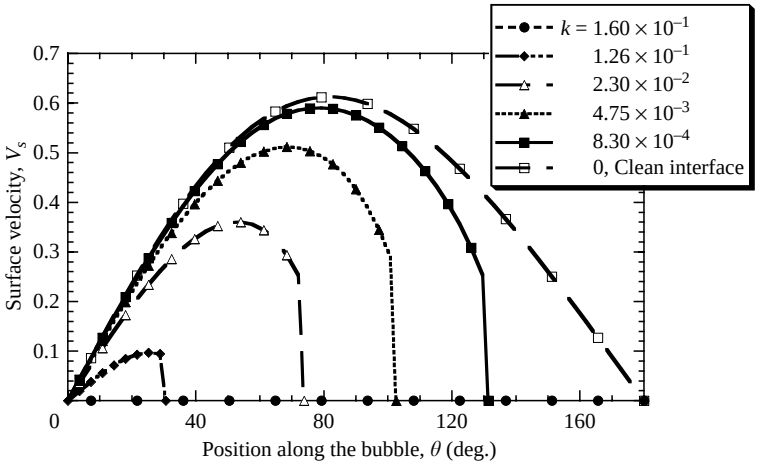

FIGURE 4. Surface velocity as a function of angle for different bulk concentrations k for a diffusion-limited case and Langmuir adsorption for parameter values as given in table 1. At the highest concentration, the interface is completely immobile.

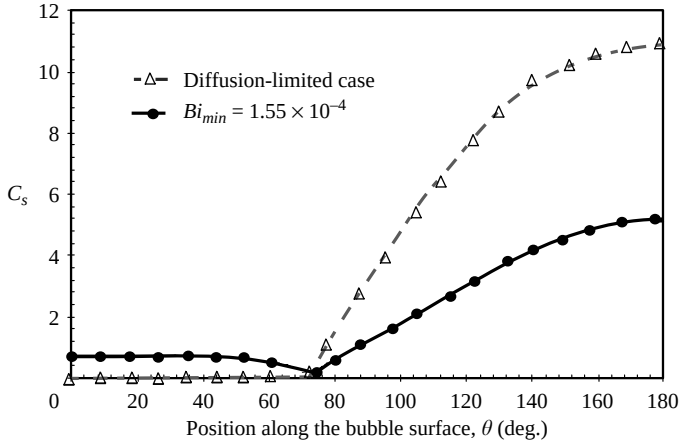

FIGURE 5. Variation of the non-dimensional sublayer concentration profile C_s for both-diffusion limited and finite-kinetic-exchange cases for Langmuir adsorption, for the same stagnant cap size, $\phi = 106.2°$, $k = 2.3 \times 10^{-2}$ for diffusion-limited and $k = 4.9 \times 10^{-2}$ for the kinetic-limited curve and other relevant parameter values are as given in table 1.

surface concentration profiles for a series of cap angles and corresponding bulk concentrations k, and figure 4 shows the corresponding surface velocity profiles. For the parameters used in this simulation, $k < 1$ and $\chi(k+1)/Pe^{1/2} \leqslant 1.271 \times 10^{-4} \ll 1$, and hence we are in the stagnant cap regime. To get a physical picture of the mass transfer mechanism we plot in figure 5 the sublayer concentration for a typical value of k, $k = 2.3 \times 10^{-2}$. It can be seen from figure 5 that at the front end of the bubble the sublayer concentration, $C_{S(Front)}/C_0$ say, is zero while that at the back, $C_{S(Back)}/C_0$ say, is in equilibrium with the surface concentration distribution. Here $C_{S(Front)}$ and $C_{S(Back)}$ denote the dimensional concentrations. Thus at the front end, surfactant diffuses towards the surface where the sublayer concentration is zero, and at the

back end surfactant diffuses away from the surface since the sublayer concentration becomes larger than the value at infinity (i.e. 1 in dimensionless terms). Note that the value of $C_{S(Back)}/C_0$ becomes of order 10^1. This relatively large value can be understood by considering the fact that at large Pe the dimensionless mass transfer at the front end balances that off the back end, at the following scales:

$$\frac{DC_0}{a}Pe^{1/2}\Phi \sim \frac{DC_0}{a}(C_s - 1)Pe^{1/3}(1-\Phi), \tag{3.1}$$

where Φ is the area of the clean part of the bubble divided by the total area. Note that at the back, and since the interface is immobile, the mass transfer scales, at large Pe, with $Pe^{1/3}$, whereas (see the Introduction) on the interfacially mobile front end the scale is $Pe^{1/2}$. When $\Phi = O(1)$, as is the case in figure 5, then $(C_s - 1)$ must be of order $Pe^{1/6}$, i.e. large, so that the diffusional fluxes balance. This accounts for the $O(10)$ value of C_s observed in the figure. For the diffusion-limited case the sublayer concentration is directly related to the surface concentration. The Γ distribution, determined by integrating the shear stress, is 0.20 or less since the Marangoni number is order 10 in this run. In general, as can be seen from equation (2.17), we have $\Gamma \sim Ma^{-1}$, and for $k \ll 1$, from the adsorption isotherm $\Gamma \sim kC_s$ and $C_s \gg 1$ and hence

$$\frac{DC_0}{a}Pe^{1/2}\Phi \sim \frac{DC_0}{a}\frac{1}{kMa}Pe^{1/3}(1-\Phi) \quad (Ma \gg 1). \tag{3.2}$$

This explains why small values of k can give rise to large stagnant caps when Ma is large.

As the surfactant bulk concentration is increased, figure 3 and figure 4 show that the stagnant cap increases. A physical explanation of this is as follows. At any given cap angle ϕ, the dimensional flux of surfactant from the bulk to the front end of the bubble scales as $DC_0Pe^{1/2}/a$ (since the surface concentration is zero and by quasi-equilibrium so is the sublayer concentration), while at the back,end the flux off the bubble surface into the bulk scales as $D(C_{S(Back)} - C_0)Pe^{1/3}/a$. Consider an increase in bulk concentration k or C_0 with the cap angle fixed. The flux at the front end onto the bubble surface increases; since the cap angle does not change, the Γ distribution and, owing to the diffusion-controlled limitation, the sublayer concentration $C_{S(Back)}$, do not change. Thus, the flux off the back end decreases with an increase in k or C_0. In order for these fluxes to balance for steady-state conditions, the cap angle must increase. From figure 3 and figure 4, we observe that small changes in k can lead to very large changes in cap angle; this is due to the fact that at such high Péclet numbers, the scaling of the flux onto the front end is asymptotically larger than that off the back. In the limit in which the stagnant cap angle tends to π, equation (3.2) indicates that the size of the clean sector scales as $\Phi \sim 1/(Pe^{1/6}Mak)$. For the values of physical parameters given in table 1, complete coverage occurs at a value of k approximately equal to 0.3.

From the dependence of cap angle on bulk concentration, we can obtain the corresponding dependence of the drag coefficient. These results are given in figure 6 which presents the scaled drag coefficient C_D^* defined as

$$C_D^* = 100\frac{\left[C_D - C_{D(Bubble)}\right]}{\left[C_{D(Solid)} - C_{D(Bubble)}\right]}, \tag{3.3}$$

as a function of k for $Re = 0$, 0.91 and 100. In the above $C_{D(Bubble)}$ and $C_{D(Solid)}$ denote the drag coefficients for a clean (stress free) bubble and solid at a particular Re. In the diffusion-limited case ($Bi \to \infty$), we observe that as more surfactant is added to

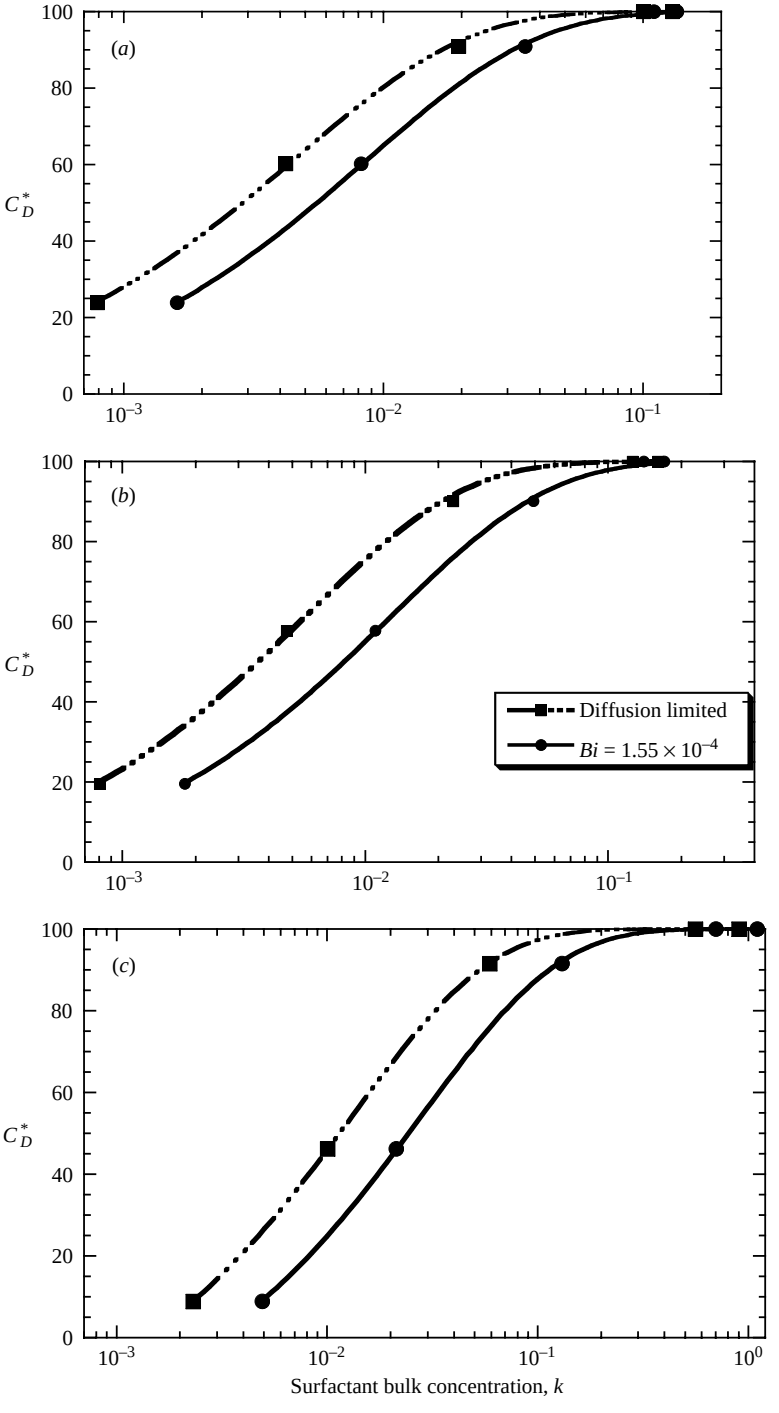

FIGURE 6. Numerical simulations showing the effect of the surfactant bulk concentration on the scaled drag coefficient of a rising bubble in the stagnant cap regime. Shown for cases when the surfactant follows a Langmuir type kinetics ($K = 0$) at (*a*) $Re = 0$, (*b*) $Re = 0.91$ and (*c*) $Re = 100$. Other relevant parameter values are as given in table 1.

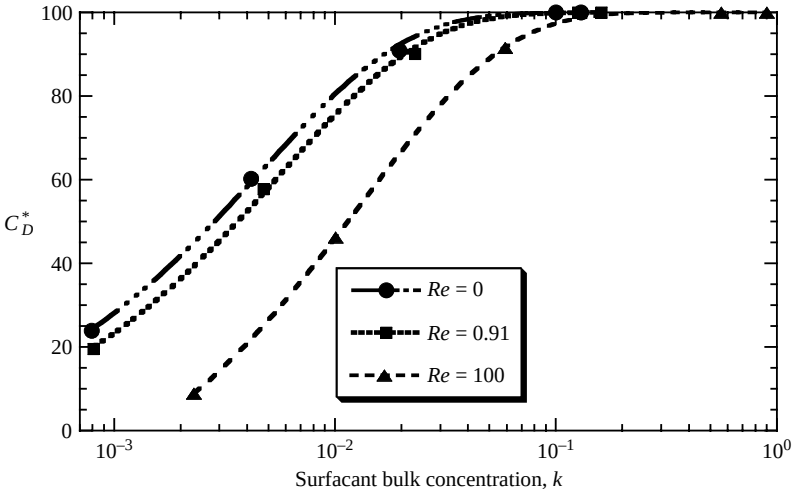

FIGURE 7. The variation of the scaled drag coefficient on a rising spherical bubble with the surfactant bulk concentration. Effect of flow Reynolds number. Shown for cases when the surfactant follows Langmuir type kinetics ($K = 0$) and when its transport is diffusion limited. Other relevant parameter values are as given in table 1.

the bulk and the size of the stagnant cap increases, drag on the bubble increases from that of a stress-free value to that of a completely stagnant interface having a solid-like value. Figure 6 also shows the drag coefficient as a function of the bulk concentration, for the case of finite kinetic Langmuir exchange rates with $Bi = 1.5 \times 10^{-4}$, and the three Reynolds numbers shown in the figure. These will be discussed further on.

Next we consider the effect of the Reynolds number on the stagnant cap size and drag for the diffusion-limited case of Langmuir adsorption. In figure 7, we plot the scaled drag as a function of k for three different Reynolds numbers, $Re = 0, 0.91, 100$. We note that as the Reynolds number increases, the curves shift to the right. This can be rationalized as follows. For a given cap angle, the shear stress $\tau_{r\theta}(\theta)$ acting over the stagnant cap region increases with Reynolds number, implying an increase in the surface surfactant concentration $\Gamma(\theta)$ necessary to balance the increased shear stress (see equation (2.17)). A higher surfactant surface concentration can only be achieved, then, by a higher surfactant bulk concentration C_0. Hence to achieve the same cap angle, a higher surfactant bulk concentration C_0 or k is required.

We note that in the stagnant cap boundary conditions that follow from (2.13), the discontinuity in shear stress at the position $\theta = \pi - \phi$ where the cap begins, is a square root singularity (see for example Harper 1973), that is $\tau_{r\theta} \sim |\theta - (\pi - \phi)|^{-1/2}$. Hence, it follows from equation (2.17) that $\Gamma(\theta) \sim \int \tau_{r\theta}\, \mathrm{d}\theta \sim |\theta - (\pi - \phi)|^{1/2}$, in the limit close to the discontinuity, $\theta \to (\pi - \phi)$. The same is true for the surface velocity $v_s(\theta)$ in the stress-free region, that is $v_s(\theta) \sim [\pi - \theta - \phi]^{1/2}$. These results are confirmed by our numerical simulations as shown in figure 8. In figure 8 we plot the surface concentration Γ and surface velocity v_s close to the stagnant cap discontinuity against the square root of the distance from the discontinuity. The linear behaviour evident in the figures for a range of cap angles chosen from the simulations confirms the above facts and acts as additional validation for the code's accuracy.

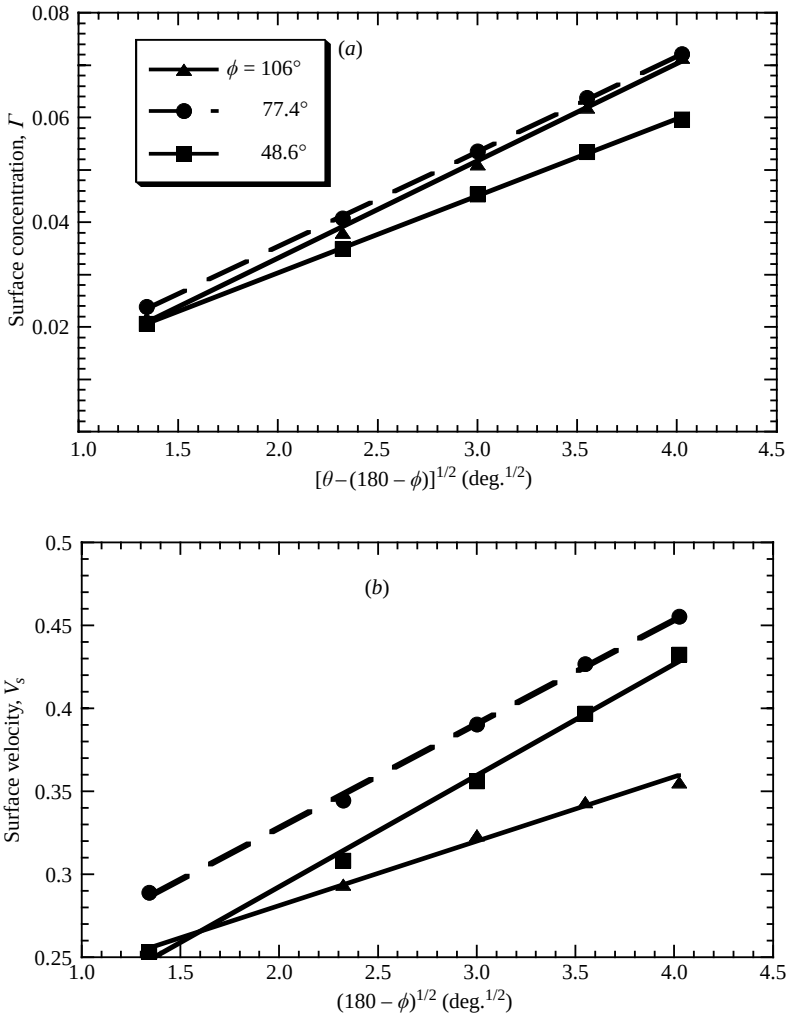

FIGURE 8. Surfactant surface concentrations (*a*) and interfacial velocities (*b*) close to the point of stagnant cap discontinuity (at $Re = 0.91$ for a diffusion-limited case). This indicates the square root singularity in the shear stress at the position of the stagnant cap. Other relevant parameter values are as given in table 1.

3.2. *Diffusion coupled with finite Langmuir or Frumkin kinetics*

Figure 6 compares the drag for the diffusion-limited case and a finite value of $Bi = 1.55 \times 10^{-4}$ (this value is selected to correspond to the minimum value of Bi in the experiments reported in § 4), for three values of $Re = 0, 0.91, 100$. We see from these results that the effect of finite kinetics is to reduce the drag, i.e. decrease the cap angle, at a given bulk concentration. Alternatively, to achieve a given cap size a higher bulk concentration is needed than in the diffusion-limited case. This can be explained as follows. Consider the diffusion-limited case with a given cap size ϕ corresponding to $k = 2.3 \times 10^{-2}$ as shown in figure 3. With the introduction of finite kinetics, the sublayer concentration profile changes, for the same surface concentration distribution, as shown in figure 5 in accordance with equation (2.8).

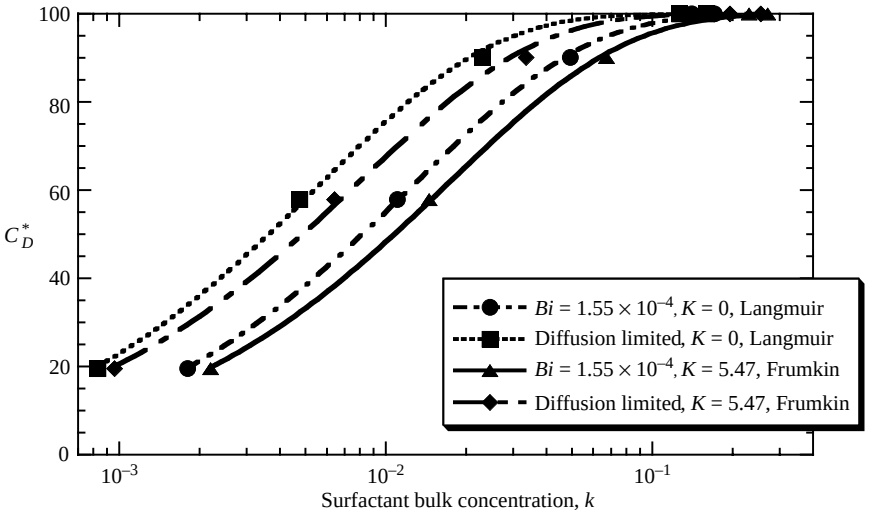

FIGURE 9. Numerical simulations showing the effect of the surfactant bulk concentration on the scaled drag coefficient of a rising bubble in the stagnant cap regime. Shown for cases when the surfactant follow Langmuir type kinetics ($K = 0$) and when it follow Frumkin type kinetics (K non-zero, here $K = 5.47$) at $Re = 0.91$. Other relevant parameter values are as given in table 1.

While at the front end $C_{S(Front)}/C_0$ increases and becomes non-zero in contrast to the diffusion-limited case, at the back end, $C_{S(Back)}/C_0$ decreases from its diffusion-limited value. These changes in the sublayer concentration reduce the bulk diffusive flux to the surface at the front end of the bubble, which scales as $Pe^{1/2}$, and from the back end of the bubble into the bulk, which is of order $Pe^{1/3}$. However, since the flux at the front scales higher with Pe than at the back, changes in sublayer concentration have a greater effect on the flux at the front end, and hence the net surfactant flux onto the bubble surface is reduced. To maintain the mass balance of the surfactant at both the front and back end (we are in a steady-state configuration), we need to increase the surfactant flux onto the bubble surface at the front by increasing the bulk concentration C_0 or non-dimensionally k.

Figure 9 presents results when the surfactant follows Frumkin-type kinetics (here $K = 5.47$ which characterizes the interaction parameter for the $C_{12}E_6$ surfactant used in the experiments and a positive value of K is typical for most surfactants (Chang & Franses 1995)). Again values of $k < 1$ satisfy the stagnant cap restriction $\chi(k + \exp K(\Gamma_o/\Gamma_\infty))/Pe^{1/2} \ll 1$. Trends similar to those for the Langmuir case are found. Notably, at any given surfactant bulk concentration k, a lower drag is achieved compared to the corresponding Langmuir case. To explain this effect for the case of diffusion limitation, consider the cap angle and hence the hydrodynamics fixed. The surface concentration computed from the stress balance changes because of the intermolecular term (K) in the equation of state (2.17). For repulsive interactions (K larger than zero), smaller values of the surface concentration are obtained for the Frumkin case at the same angular position in the cap because surface pressures are much larger due to the intermolecular contribution. The sublayer concentration in equilibrium would then nominally be smaller due to the lower surface concentration. However this effect is offset by the fact that, with repulsive intermolecular interactions, to achieve the same surface concentration much larger equilibrium bulk concentrations

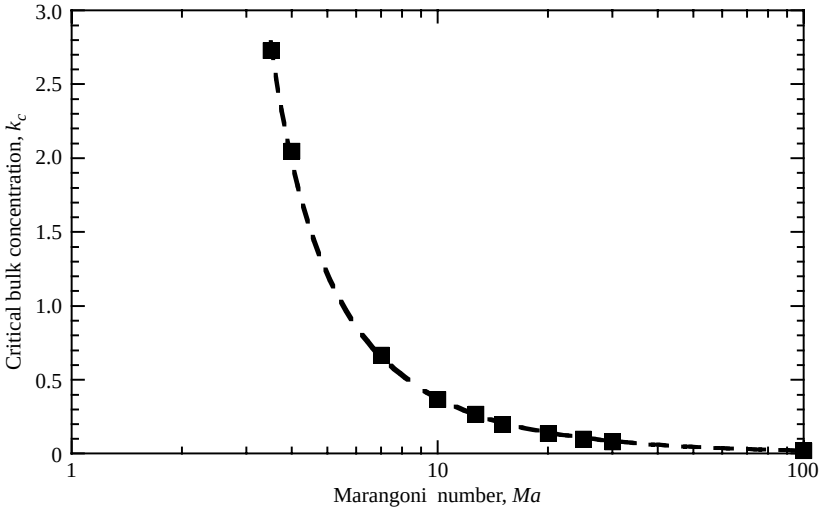

FIGURE 10. Effect of the Marangoni number on the amount of surfactant, k_c, needed for the stagnant cap to completely cover the bubble surface – diffusion-limited case for $Re = 0.91$, $K = 5.47$. Other relevant parameter values are as given in table 1.

are necessary, so the local equilibrium surface concentrations are much greater than those for the Langmuir case. As a consequence, there is greater desorption off the back end for the Frumkin case. The front end is unaffected since the surface concentration is equal to zero. The bulk concentration should then be increased to reduce the diffusive transport off the back end and allow the Nusselt number to be equal to zero. Inclusion of a kinetic limitation reduces the drag relative to the diffusion-limited case for the reasons discussed earlier of the large reduction in the adsorption at the front end, and this is true for the Frumkin model as well so the Frumkin curves lie below their diffusion-limited simulations.

In figure 10, we plot the bulk concentration (k_c) of surfactant needed to create a stagnant cap that covers the entire bubble surface (cap angle $\phi = \pi$), as a function of the Marangoni number Ma, for the case of a diffusion-limited surfactant transport following Frumkin exchange kinetics (with the value of K as specified earlier). We see that as the Marangoni number increases, complete coverage is achieved at lower surfactant bulk concentrations. Physically, from the definition of the Marangoni number $Ma = \mathscr{R}T\Gamma_\infty/\mu U$, smaller sized bubbles have higher Marangoni numbers. It can be concluded, therefore, that smaller bubbles are completely covered and behave like solid spheres at lower bulk concentrations than larger sized bubbles. This behaviour is observed in our experiments which are described in § 4 of this study. We also note that the results of figure 10 explain the findings of Zhang & Finch (2001), Zhang *et al.* (2001). These authors measured the terminal velocities of bubbles in an aqueous Triton X-100 surfactant solution, and found that for the concentration range they employed ($10^{-3} - 10^{-5}$ mol m^{-3}) the bubbles rose with a velocity independent of concentration. We estimate a Marangoni number of approximately 70 for their experiments ($2a = 0.8$ mm, $U = 0.1$ m s^{-1}, $\mu = 10^{-3}$ kg m^{-1} s^{-1}, $\Gamma_\infty = 2.91 \times 10^{-6}$ mol m^{-2} (Triton X-100 at the air/water interface)), and using figure 10 provides a minimum concentration of $k_c = 0.05$ which corresponds to a bulk concentration of about 3×10^{-5} mol m^{-3}; this value is in turn approximately equal to the minimum value used in the experiments of Zhang *et al.* (2001). The reason why their velocities

were independent of concentration may therefore be that their concentrations are above the critical value given in figure 10. (Note that this is an estimate because figure 10 was obtained for a Reynolds number of 0.91 whereas their value is approximately 40. In addition, their value of Pe is one order of magnitude smaller and $K = 0$, whereas χ is approximately the same.)

Above k_c, the stagnant cap extends over the entire surface of the bubble. Further increases in bulk concentration increase the amount adsorbed onto the surface with the concentration at the front pole increasing from zero. The hydrodynamics will not be changed as long as the diffusive transport rates (to/from the bulk) and the kinetic exchange rates (at the interface) of the surfactant do not outweigh the surface convection rate. When bulk concentrations are large enough that the kinetic or diffusive rates become of the order of the convective rate, then we enter the uniformly retarded and remobilization regimes. There are no sharp gradients in shear stress, or surface concentration, on the bubble surface in these regimes. To find the drag on the bubble as a function of the surfactant concentration in these regimes, the complete flow equations (2.1) and (2.2), coupled with the surfactant transport equations in both the bulk (2.3) and on the surface (2.7), must be solved simultaneously. The coupling occurs through the shear stress balance on the surface as given by equation (2.6) (see Wang *et al.* 1999).

4. Experiments

4.1. *Materials and experimental apparatus*

We originally intended to measure the velocity of gas bubbles in aqueous surfactant solutions since the adsorption properties of surfactants at the air/water interface have been well-studied (Borwankar & Wasan 1983; Chang & Franses 1995) and comparison with the theory (which requires the adsorption constants) could be made. However, for air bubbles in the size range we are interested in, i.e. of radii 0.1–1 mm, steady rise velocities in water, as experimentally measured by several investigators (see for example Clift *et al.* 1978), are of the order 10–400 mm s^{-1}. At the higher velocities in this range, inertial effects are of the order of capillary forces (i.e. We approaches 2) so the bubbles with the larger radii, as has been observed, are deformed. Our theory is for spherical shapes; since we want to quantitatively compare the theory to these experiments, we decided to increase the continuous-phase viscosity (μ) by adding glycerol to water to reduce U. We chose a glycerol/water ratio of 7:3 by volume, which has a viscosity of 29 cP (as measured by a Haake Couette viscometer), and a density of 1.192 g cm^{-3} (as measured by a Troemner densiometer) at 25 °C. As we will verify (see also Maxworthy *et al.* 1996), gas bubbles in the range of 0.3–0.8 mm in radius rise with velocities of the order of 10–60 mm s^{-1} keeping the Weber number less than 0.05, so that the bubbles remain spherical.

In preparing the continuous phase, the water is purified from tap water using a Millipore Q System (Millipore, MA) with a specific resistance greater than 15 M ohm cm. The glycerol is obtained from Sigma and is used without modification. The surface tension of the aqueous/glycerol mixture against air was equal to 65.6 dyn cm^{-1} as measured by a pendant bubble apparatus. For extended times, the tension reduced by less than 1 dyn cm^{-1}, indicating that the impurities in the mixture were at very low concentration. In the range of temperatures studied (24–27 °C), the density of the solution did not vary but the viscosity is a strong function of temperature and its effect is accounted for in our study. Viscosities were measured at various temperatures in the range 24–27 °C, and these data were then used to obtain a

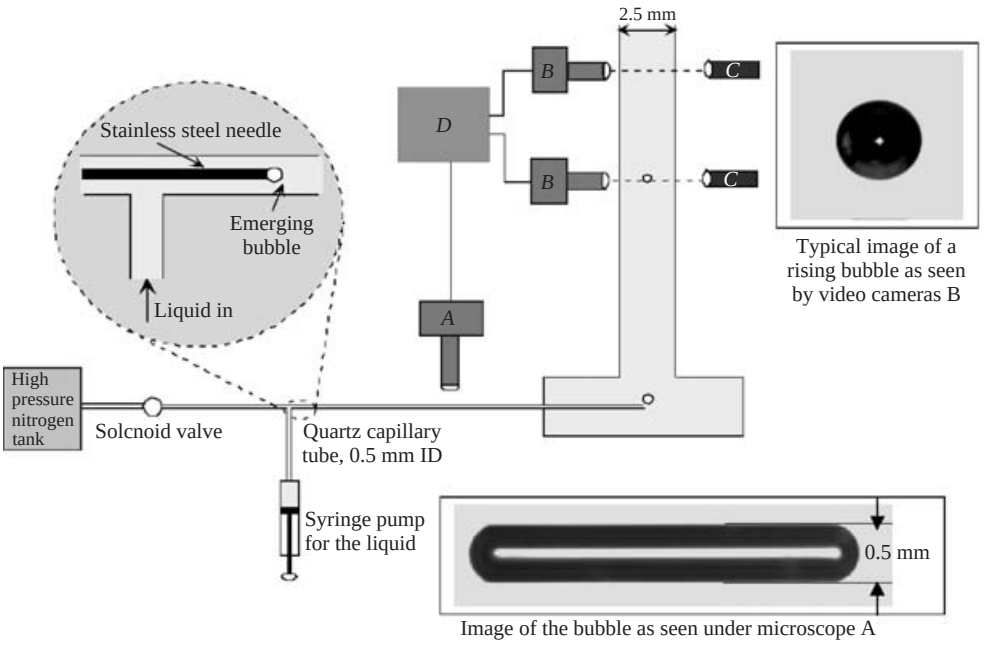

FIGURE 11. Experimental apparatus for the measurement of bubble rise velocities. A, microscope; B, video camera; C, light source; D, Mac w/Frame grabber. Insets show the details of the manufacture of the sub-millimetre sized bubbles, and video captures of the bubble slug in the capillary and the spherical, rising bubble in the chamber.

correlating polynomial for the variation of viscosity with temperature. In computing the experimental drag coefficients, the polynomial was used to obtain the viscosity at the temperature of the experiment, and this value was then used in calculating the coefficient (see below).

For the present study, we chose the non-ionic polyethoxylated surfactant $C_{12}E_6$, with the following structure ($CH_3(CH_2)_{11}(-OCH_2CH_2)_6-OH$) and a molecular weight of 450.7. This was obtained from Nikkol Surfactants, Japan; from gas chromotography, samples of these surfactants were shown by the manufacturer to be better than 99.9 % pure.

The experimental apparatus we designed to measure bubble rise velocities is given schematically in figure 11. The apparatus consists of two parts: a horizontal capillary tube where the bubbles are created, and a vertical chamber filled with the continuous liquid phase and connected to the tube, in which the bubbles rise and their velocities and shapes are measured by video recording. A train of gas bubbles is created in a horizontal precision bore quartz capillary tube 0.5 mm in bore (Wilmad Glass, NJ) by injecting nitrogen into a flowing stream of the continuous liquid phase. The stream is driven by a syringe pump and enters the capillary tube at the T junction. The stream flow is set up first. Pressurized nitrogen is connected by teflon tubing from a tank to a stainless steel needle inserted in the capillary tube 1 cm past the T junction. The outer diameter of the needle (0.45 mm) fits loosely into the capillary bore, allowing the continuous liquid phase introduced at the T to flow in the annular space between the needle and the inside surface of the capillary tube. The inner diameter of the stainless steel needle is 0.25 mm. Between the tank and the capillary tube is a miniature solenoid valve (Lee Co., CT). Initially the valve is closed, and then is rapidly opened

and closed by application of an electronic pulse. The nitrogen, which is pushed into the stream, flows out of the needle; as it emerges from the needle's tip, it is broken into small segments by the liquid flow. The sizes of the gas segments formed can be controlled by adjusting the gas and liquid flow rates. We find that with this tube insert we can form segments with equivalent spherical radii as low as 0.3–0.8 mm. After the segments are created, the flow is stopped and one segment is observed under magnification with a stereo microscope (Nikon, NY).

To obtain magnified images of the slugs in the capillary, the capillary is placed horizontally in a petri dish filled with water in order to minimize optical distortion, and the objective of the microscope is positioned above the capillary. The index of refraction of the water on the outside of the capillary, and of the glycerol/water mixture on the inside, is approximately equal to that of the capillary wall so that the wall of the tube nearly disappears in the magnified image and the curvature of the capillary does not distort images of the slug in the radial compared to the axial direction. The slug appears dark due to the difference in indices of refraction between the air and the glycerol/water mixture. An example is given in the inset of figure 11. The mixture generally wets the inside surface of the quartz capillary (though not always perfectly, see below) so the slug in the magnified image is composed of a cylindrical plug with two ends which resemble outwardly extending sections of spheres (gravitational effects have a negligible effect on the menisci shape for our small bore capillary).

The microscope image is video recorded using a CCD camera (Dage MTI, IN) and digitized (using a VG-5 Scion Frame Grabber on a Macintosh G3 computer with a pixel resolution of 640 (horizontal, along tube axis) $\times$ 480 (vertical, perpendicular to the axis)) to obtain a digital image. The volume of the slug is computed from the digital image as the sum of two terms. The first is the volume of the plug section and is obtained by multiplying the length of the slug by $\pi(r_c)^2$ where r_c is the radius of the capillary. The radius of the precision bore capillary is 0.5 mm accurate to less than 0.1 % (information as provided by the manufacturer). (Note that we ignore any contributions to wetting layers surrounding the slug; these layers develop as the slug moves. When the slug is stopped the wetting layer drains to the bottom of the capillary as the gas slug rises to the top of the tube and contacts the wall. This residual liquid is then removed by capillary pressure since the pressure in the liquid underneath the long horizontal plug is of order $1/r_c$ less than the gas slug pressure while the pressure at the ends is of order $2/r_c$ less than the gas pressure. We wait a few minutes for the liquid to drain.) The length of the slug is obtained by scanning pixel-by-pixel the intensity in a direction along the tube axis at the inside diameter of the tube to locate the contact points of the menisci with the wall. A calibration recticule is used to obtain the pixels mm^{-1} calibration factor and convert the length in pixels to physical dimensions; in this recticule, ruler markings separated by 2 mm in the horizontal direction digitally span approximately 200 pixels and are used to obtain the calibration factor. The second contribution to the slug volume are the volumes V_{end} of the sections of the spheres and are given by

$$V_{end} = \pi \frac{1}{\cos^3 \theta_c} {r_c}^3 \left[\frac{2}{3} - \sin\theta_c + \frac{\sin^3 \theta_c}{3} \right] \tag{4.1}$$

where θ_c is the contact angle the glycerol/water mixture subtends with the capillary wall as measured through the liquid phase. The contact angles are measured by either inspection of the intersection of the meniscus with the capillary, or by fitting

the meniscus to a circle, computing the radius of the circle, r_t, and determining the contact angle from $\cos(\theta_c) = r_c/r_t$. For pure glycerol/water mixtures, or mixtures with very low concentrations of surfactant ($< 10^{-1}$ mg l^{-1}), the contact angles are equal to zero as the mixture wets the capillary wall, and the ends of the slug are hemispheres. In this case, the volume is calculated assuming a slug shape consisting of hemispheres with radius r_c at the ends of a cylindrical section. However for higher concentrations, the contact angle as measured from the images is non-zero and the exact formula for the ends of the slug is used. It is important to note that the contributions due to the hemispherical ends are an important portion of the entire bubble volume.

From these details of the calculation of the bubble volume, we can also estimate the error in the measurement of the equivalent spherical radius. For the clean bubbles, and bubbles in a continuous phase with concentrations less than or equal to 10^{-1} mg l^{-1}, the contact angles are zero and the contributions of the end caps to the volume are accurately described as $\frac{4}{3}\pi r_c^3$. The errors in the volume measurement result from the error in the measurement of the slug length which varies from 25 pixels (for the 0.3 mm bubbles) to 400 pixels (for the 0.6 mm bubbles). (The bubbles in the range of 0.7 mm to 0.8 mm were imaged under a lower magnification but with equal accuracy as the 0.6 mm bubbles.) The menisci intersections in the measurement of the slug length can be located to within a pixel at either end; so the error in the length varies from ± 8 % for the 0.3 mm bubbles to ± 0.5 % for the 0.6 bubbles. The calibration factor has a similar error of 2 pixels in 200 or 1 %, so the error in the calculation of the length of the bubbles in millimetres is approximately 9 % for the 0.3 mm bubbles down to 1.5 % for the bubbles in the range of 0.6–0.8 mm. Thus the error in the measurement of the equivalent spherical radius is 1/3 of these errors or approximately 3 % for the 0.3 mm bubbles down to less than 1 % for the 0.6–0.8 bubbles. For the higher surfactant concentrations for which only bubbles in the range of 0.6–0.8 mm were used, the contact angles were not zero so the error in the measurement of the contact angle will propagate to the calculation of the endcap volume. However the endcap volumes are 10 % or less of the total volume for the 0.6–0.8 mm bubbles, so their error is not as important as the error in the volume of the cylindrical plug, and the error in the equivalent radius is again less than 1 % as it was for the surfactant-free bubbles 0.6 mm–0.8 mm in radius. The radii used in the calculation of the drag coefficient (see below) is corrected for the expansion of the gas bubble due to the decrease in the hydrostatic pressure as the bubble rises in the chamber.

Once the bubble has been formed and its volume measured, the syringe pump is used to push the test segment out of the capillary and into the vertical chamber where it begins to rise. The chamber consists of a vertical quartz tube, 25 mm in diameter (Wilmad Glass, NJ) and 70 cm in length. The upper part, where the bubble motion is recorded, is of square cross-section to minimize optical distortion. To minimize surfactant contamination, care is taken in the selection of all the materials for the apparatus so that the experimental fluid comes in contact with only stainless steel or teflon, or a viton polymer (equilibrated with the liquid being used). Contact with the surrounding air is also minimized, and all glassware is cleaned with Nochromix. Since the viscosity of the liquid being used is a function of temperature, the temperature is carefully monitored in the course of the experiment by a probe dipped in the quartz cell.

For velocity measurements, the bubble motion is recorded with two CCD cameras (Dage MTI, IN) located a known distance apart (170 mm). The first camera is located at a height of approximately 55 cm above the tip of the capillary tube from where the bubble starts to rise. A parallel beam of light from a collimating lens provides the

back lighting for each camera. The lens on the camera is a Cosmicar television lens f/1.4 25 mm adjusted to a magnification such that the field of view is approximately 5 mm. Both these cameras are connected to the VG-5 Scion Frame Grabber on the Macintosh G3. Instantaneous bubble velocities can be measured at each of the two locations by capturing successive digital images (480 (in the direction of motion of the bubbles) $\times$ 640 pixel resolution) while the bubble remains in the field of view of the camera and tracking the motion of the centre of mass. The cameras digitize images every 1/30 s (times of capture for each image, from a common starting point for both cameras, are printed on the digitized video frame by the frame grabber board and are accurate to much less than 1 %). The even and odd line compositions of the capture are executed in half that time or 1/60 s, and we use the even or odd compositions to locate the bubble position and centre of mass. Bubbles travel with a velocity of approximately 10 mm s^{-1} (for the 0.3 mm radius bubbles) to 60 mm s^{-1} (for the 0.8 mm radius bubbles) (see figure 12) so bubbles move a distance of 1/6 mm to 1 mm during the capture. This could lead to blurring; however the cameras are equipped with electronic shutters with speeds up to 1/50 000 s which were used to reduce the blur. An example of the video captured image of the rising bubble, demonstrating the clear focus, is given in the inset of figure 11. The field of view in the cameras is approximately 5 mm so the minimum time the bubbles are in the field of view is 5/60 s, and on average there are at least 5 frames (even or odd) captured for each passage of the bubble. To measure the instantaneous velocity, the first and last frames of the bubble in the field of view are used; the centres of mass are on average separated by half the field of view or 120 pixels (since even and odd fields have verical spans of (1/2)480 pixels), and with an error to locate in the centre of mass of one pixel each, the error in the velocity is 2/120. The digitized images were calibrated by using spheres of known size; these spheres of 1.5 mm in diameter (accurate to better than 0.1 %) scanned approximately 160 pixels in diameter (full field since a static measurement) so the error in the calibration measurement is 2/160 % and the error in the instantaneous velocity measurement is 3 %.

Average terminal velocities are measured by dividing the distance between video cameras by the time elapsed between captures of the bubbles on the cameras. Markings on the chamber are in the field of view of each camera; the distance between these markings is 170 mm and is measured accurate to within 1 mm. As a bubble rises, each camera records (with even or odd line composition) at least five bubble frames. The centres of mass are located to within a pixel, and the distance between the centre of mass and the marking in the field of view is measured in pixels and converted to millimetres (with submillimetre accuracy). To compute the average velocity we divide the distance between the bubbles (as obtained by noting the distance the centres of mass are from the markings) by the recorded time; since the accuracy in the marking measurement is 1/170, the error in the velocity is approximately 1 %, which is smaller than the 3 % error in instantaneous velocity. The instantaneous velocities are compared with the average to verify that the bubble has reached a terminal velocity; in practice the average and instantaneous velocities are within one or two percent of each other verifying that steady state has been achieved.

From the digitized images, the radius of the bubble can also be directly calculated, although with an error greater than that realized from the microscope measurement. The diameter measured by the video cameras capturing the bubble motion is of the order of 30 pixels for the smallest sized bubbles to 85 pixels for the largest bubbles. The error therefore in the radius ranges from 2 % to 7 % (assuming a one pixel error in the measurement of the diameter at either end of the bubble), and with

an error of 2/160 in the calibration, so the composite error in the measurement of the radius in approximately 3–8 %. This compares with an error of less than 1–3 % for the microscope measurement. Nevertheless after correction of the microscope measurement for expansion, the radii of the bubbles as measured with the microscope in the capillary were always within a few percent of the measurement by the cameras tracking the bubble motion.

In the experiments reported it is important that the bubbles reach a steady-state velocity in order to compare with the calculations of the steady-state velocity. While we noted above that verification is obtained by comparing the average and instantaneous velocities, several other studies confirm that the bubble rise distance of 55 cm to the first camera is large enough to allow the bubbles to come to steady state. Simulations of the unsteady motion of clean bubbles by Liao & McLaughlin (2000*a*) for Reynolds numbers between approximately 55 and 260, indicate that the time scale to steady-state decreases from $60a/U$ to $40a/U$ for Re ranging from about 260 to 55. As our experiments have $Re = O(1)$, the time scale is smaller than that computed in Liao & McLaughlin (2000*a*). In our experiments the time to reach the first camera is of order L/U, where L is the distance the bubble travels before the first measurement is taken and is 55 cm; thus the ratio of the hydrodynamic equilibration ($40a/U$ or less) to L/U is $40a/L$ which is less than 0.1.

As a last consideration, the bubbles translate in a chamber and we need to examine any corrections of rise velocities due to the walls because we compare experiments with simulations with an unbounded geometry. The diameter of the chamber is 25 mm and for the measurements reported in this paper the largest bubbles are 1.6 mm in diameter giving a maximum aspect ratio $\lambda = 0.06$. Clift *et al.* (1978) report a correction to the terminal velocity for $\lambda = 0.6$ and $Re = O(1)$ less than 2 %, so that we can safely neglect wall effects.

The drag coefficient is obtained from the velocity measurement by equating the buoyancy force to the hydrodynamic drag (formulated as the drag coefficient multiplied by the normalizing scale $2\pi\mu a$):

$$C_D = \frac{2a^2\rho g}{3\mu U}. \tag{4.2}$$

Densities (as measured with the Troemner densiometer) are accurate to 1 % and viscosities (as measured using a Haake Couette viscometer) are accurate (judging from the reproducibility of the measurements) to within 1 %. With errors in the terminal velocity of 1 % (we use the average velocity and radius as measured at the microscope station), a composite error of 5 % in the drag is realized (as the bubble radius enters as the square in the formulae) for the 0.6–0.8 mm bubbles. For the clean, smaller bubbles the error approaches 9 % for bubbles of radii 0.3 mm.

4.2. *Measurements of terminal velocities for surfactant-free bubbles*

Our first step is to use our apparatus to measure bubble rise velocities in the absence of surfactants dissolved in the continuous phase, and to compare these results with previously established theoretical ones. A successful comparison indicates that our cleaning procedures are adequate, and all calibrations are accurate. These results also form a basis for our subsequent experiments in which surfactant is added to the continuous phase. In figure 12 we show the rise velocities of bubbles plotted as a function of their size. These velocities are the average of the three values: two instantaneous velocities from the two cameras at two different heights and the third from the time of rise of the bubble between the two. Since these measurements differ

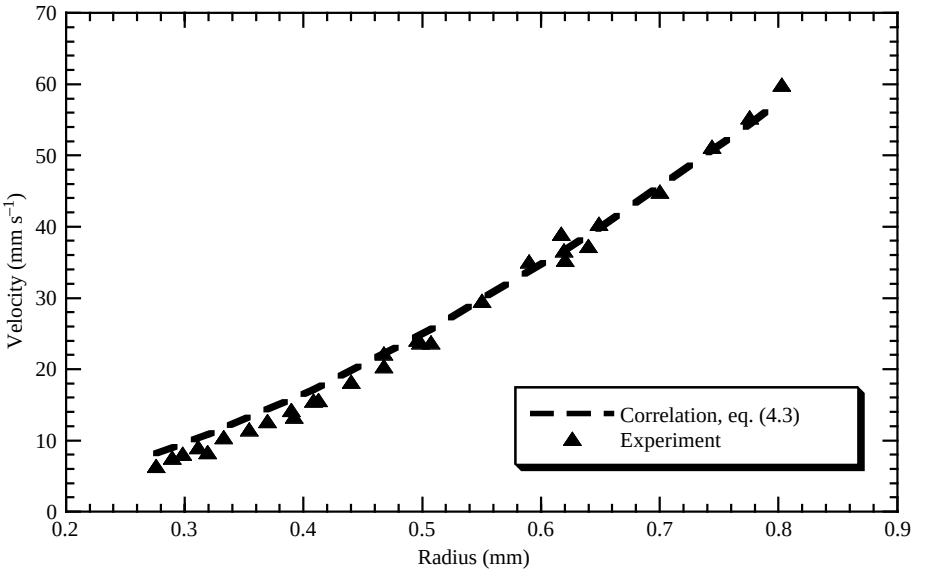

FIGURE 12. Bubble rise velocities in a surfactant-free 70:30 glycerol/water mixture (▲). Comparison with the theoretical prediction by equation (4.3) shown by the dashed line.

by one or two percent, we conclude that these bubbles have reached their steady state. We note that the Weber and capillary numbers (*We* and *Ca*) for these bubbles are of order 10^{-2}, while the Reynolds number *Re* is of order 1. So we do not expect to see any inertial or viscous effects deforming the bubbles. This is confirmed by the video images of the rising bubbles (see the inset of figure 11), which indicate spherical shapes.

Also plotted in figure 12 are the predicted rise velocities of these bubbles from the numerical work of Magnaudet, Rivero & Fabre (1995). A correlation for the drag coefficient $C_{D(Bubble)}$ from their simulations (but using the viscous scale for the drag coefficient) for a spherical bubble is given by

$$C_{D(Bubble)} = \frac{2a^2\rho g}{3\mu U} = 2(1 + 0.15(2Re)^{0.5}). \tag{4.3}$$

The predicted velocities are obtained by solving this equation for U. From the same reference the drag coefficient for a solid sphere $C_{D(Solid)}$ is given by

$$C_{D(Solid)} = \frac{2a^2\rho g}{3\mu U} = 3(1 + 0.15(2Re)^{0.687}). \tag{4.4}$$

We note that only bubbles of sizes greater than 0.5 mm rise with velocities agreeing with the predicted values. Smaller sized bubbles rise with velocities less than the predicted values, but larger than those for corresponding solid spheres, because of the presence of trace amounts of impurities present in our system despite our thorough cleaning procedure. Hence, we only consider bubbles of sizes greater than 0.5 mm radius. Maxworthy *et al.* (1996) also investigated the rise velocity of air bubbles in ostensibly clean glycerol/water mixtures of varying compositions. They found similar results to ours, i.e. only sufficiently large bubbles had drag coefficients in agreement with the clean interface correlations.

4.3. *Experimental results*

In this section we report measurements of the drag coefficient as a function of the bulk concentration of the surfactant $C_{12}E_6$. The experiments are done for low concentrations equal to 10^{-3} mg l^{-1} to around 10^3 mg l^{-1} (10 times the CMC of the surfactant). For the $C_{12}E_6$ surfactant we have measured the equation of state and the dependence of the surface tension on the bulk concentration by using the pendant bubble technique for the air/glycerol–water mixture, and have fitted these data to the Frumkin equation of state (2.5) and the adsorption isotherm $\Gamma_o/\Gamma_\infty = (\beta C_0/\alpha)/((\beta C_0/\alpha) + \exp(K\Gamma_o/\Gamma_\infty))$ which follows from equation (2.8) under equilibrium conditions, to obtain values of K, Γ_∞ and the ratio α/β. These values are given in table 1. In addition, dynamic surface tension experiments were undertaken to obtain values for the diffusion coefficient and the kinetic constants. In these experiments, the relaxation in tension as surfactant adsorbs onto an initially clean pendant bubble interface was measured, and compared to predictions from solutions to the surfactant mass transfer in order to obtain measurements of the transport coefficients. Only a lower bound could be established for the kinetic rate constants due to the fact that the high viscosity of the solution reduces the diffusion coefficient and makes the diffusion process rate-limiting. These lower bound values are also given in table 1, and the experiments are reported in Palaparthi, Papageorgiou & Maldarelli (2006). For all the experiments reported here the value of $\chi(\exp(K\Gamma_o/\Gamma_\infty) + k)/Pe^{1/2}$ is much smaller than one and so the diffusion limitation alone places these experiments in the stagnant cap regime. Values of the Biot number are dependent upon the desorption rate constant, and the lower bound we have measured gives a minimum value for the Biot number of the order of 10^{-4}. Hence, even if the kinetic rates are a few orders of magnitude larger, the Biot number is still small. Thus, kinetic limitations also force the bubble motion into the stagnant cap regime.

Figure 13 plots the drag coefficient C_D (divided by the drag coefficient for a solid sphere $C_{D(Solid)}$ as given by equation (4.4) for the same Re) as a function of surfactant bulk concentration for different bubble radii, where the drag coefficient C_D is calculated from equation (4.2). At each concentration, a data point with a prescribed bubble radius represents the average of the drag coefficients of bubbles with bubble radii within $\pm 2\,\%$ of the stated value. The results show the typical qualitative behaviour we would expect from the theory, see for example figure 6. In particular $C_D/C_{D(Solid)}$ increases from that of a clean bubble (i.e. approximately 0.6), through intermediate values (corresponding to partial stagnant caps of increasing size) and reaches the value for a completely immobile, surface (i.e. 1). These results verify that partial stagnant caps whose size increases with bulk concentration can be observed experimentally. As we summarized in the Introduction, measurements of terminal velocities of rising air bubbles in surfactant solutions usually report velocities corresponding to completely rigid surfaces. The present experiments demonstrate that if the surfactant concentrations are sufficiently low and impurities are removed, bubble velocities corresponding to partial caps can be achieved. We also note from these experiments that at any given surfactant bulk concentration where there is a significant separation in the scaled drag (concentrations less than 0.1 mg l^{-1}), smaller sized bubbles behave more like solids than larger sized bubbles. As mentioned earlier, smaller bubbles, simply because of their small radii, have reduced clean terminal velocities and correspondingly larger Marangoni numbers relative to larger bubbles. As a result of the larger Ma for the smaller bubbles, the cap angle is larger and the corresponding drag coefficient is increased relative to that for larger bubbles. We also note that at the lowest two concentrations studied, we could expect a change in the bulk concentration of the surfactant solution due to the adsorption of the surfactant at the air/liquid and liquid/glass

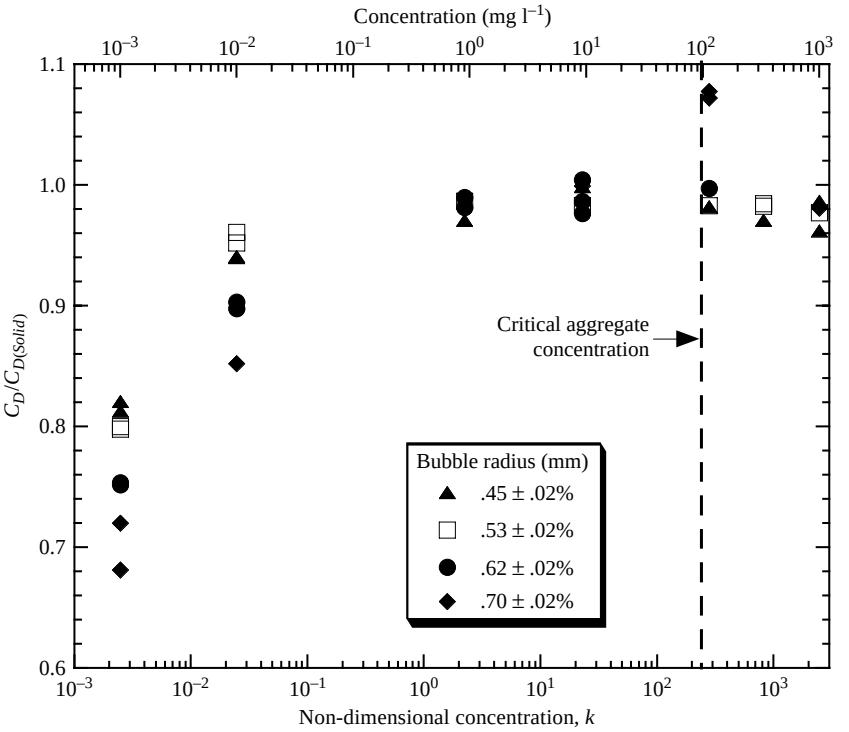

FIGURE 13. Effect of the surfactant concentration ($C_{12}E_6$) on the drag coefficient (divided by the drag coefficient for a solid sphere $C_{D(Solid)}$ at the same Re as given by equation (4.4)).

interfaces of our apparatus. We calculated this change in the bulk concentration of the surfactant as $\Gamma_\infty A_c / V_c$, where A_c and V_c are the total surface area and volume of the vertical chamber where the bubbles rise. With the surface area/volume of our apparatus of $0.0155\,\mathrm{m}^{-1}$, and $\Gamma_\infty = 4.48 \times 10^{-6}\,\mathrm{mol\,m}^{-2}$, the change in the bulk concentration becomes $6.94 \times 10^{-8}\,\mathrm{mol\,m}^{-3}$ (or $3.13 \times 10^{-5}\,\mathrm{mg\,l}^{-1}$) which is two orders of magnitude less than the smallest concentration used here. Hence this change is negligible.

We can compare the experiments quantitatively to the theory in the following ways. The average values for the non-dimensional groups corresponding to the experiments in figure 13 are those tabulated in table 1, and these were used in the simulations. The exact values of the groups for a particular bubble rise experiment differ from the average values because different sized bubbles were used, and a range in velocities was measured (as well as variations in viscosity due to the fact that the temperatures were not the same for each experiment). We note that using the average values, the simulations predict for diffusion-limited conditions that the critical concentration necessary to completely immobilize the interface is approximately 0.3 from figure 10, which dimensionally corresponds to a concentration of $0.12\,\mathrm{mg\,l}^{-1}$. The inclusion of kinetic effects will increase this value (figure 9). From figure 13 we note that the bubble interfaces become completely stagnant at approximately $0.1\,\mathrm{mg\,l}^{-1}$, in qualitative agreement. Given the fact that the behaviour of the scaled drag coefficient with concentration has a near zero slope as the completely rigid surface is approached (the scaled drag coefficient for diffusion-limited transport changes from 95 to 100 over a range in k from 0.06 to 0.3, figure 9) and the drag coefficient is measured to within 5 %, a more quantitative comparison is not possible. However, a more quantitative comparison of theory and experiment can be undertaken at concentrations for which

Radius (mm)	Re	Ma	$Pe \times 10^6$	χ	C_D Measured	C_D theoretical values $Bi \to \infty$	$10 \times Bi_{min}$	Bi_{min}
$k = 0.0024$								
0.611	0.83	10.4	1.34	0.124	2.73	2.65	2.61	2.42
0.626	0.88	10.0	1.42	0.127	2.76	2.63	2.59	2.40
$k = 0.024$								
0.619	0.81	12.2	1.3	0.125	3.27	3.42	3.40	3.19
0.605	0.76	12.6	1.24	0.123	3.23	3.43	3.43	3.22
0.635	0.83	11.5	1.34	0.129	3.27	3.39	3.36	3.18

TABLE 2. Comparison of measured drag coefficients with theoretical computations.

the cap angle is much less than 180°, and the drag coefficient is not asymptotically approaching the solid value. This comparison can also be used to understand the role of kinetics. We focused on the two lowest concentrations ($k = 0.0024$ and 0.024) in the experiments reported in figure 13, and we choose the experiments with Reynolds numbers that are approximately within 10 % of 0.91. Recall that the value of 0.91 was used in our numerical fluid mechanical simulations to calculate the drag coefficient as a function of the cap angle. Note also that a change in Re of 10 % around $Re = 0.91$ has a negligible influence on the scaled drag coefficient (see figure 7). The bubble radii selected which meet this criterion are listed in table 2. For each experiment, the Reynolds, Péclet, Marangoni and χ parameters are computed and tabulated. For each set of these parameters, the value of k corresponding to selected values of the cap angle (and therefore drag coefficient) are computed as described in the Appendix. This results in plots of the drag coefficient as a function of k as given for example in figure 6. By interpolating these plots the drag coefficient for the particular k of the experiment is obtained and tabulated in table 2 for diffusion-limited conditions, a Biot number (Bi_{min}) corresponding to the lower bound for α found from dynamic tension experiments (see table 1), and a value of Bi ten times this minimum.

Consider first the lower concentration, $k = 0.0024$. Table 2 shows that the measured drag coefficient is consistently larger than the diffusion-limited value obtained from the simulations, even accounting for the variation due to the 5 % error in C_D. Since surface kinetics can only decrease the drag coefficient, this result indicates that at this very low concentration the bubbles may be influenced by contamination and the effective value of k is larger than that due solely to the addition of the polyethoxylated surfactant. For the higher concentration ($k = 0.024$), the measured drag coefficient lies between the dynamic-tension-determined value for the minimum value of the Biot number ($Bi = Bi_{min}$) and $10 \times Bi_{min}$, suggesting strongly that kinetics is important in the effect of surfactant on the retardation in the bubble motion, and providing a finite bound for the kinetic rate constants. We have estimated the error in the measurement of the drag coefficient as ± 5 % which is a value of approximately 0.16. As this value is approximately equal to the difference in the drag coefficients for Bi_{min} and $10 \times Bi_{min}$, only a finite bound for Bi can be achieved. In general, however, these results suggest that measurements of velocities of bubbles with stagnant caps can be used as a paradigm to measure the kinetic rate constants in cases where (as here) they cannot be resolved in dynamic tension experiments. In the dynamic tension experiments for the system used here, the relaxation in tension was measured as surfactant adsorbs onto an initally clean pendant bubble interface. The surfactant transport was modelled, and from comparison of the predicted tensions to the simulations, the process was shown to be diffusion controlled (Palaparthi *et al.* 2006). A lower bound for the

kinetic constants was established by determining the value of the kinetic constants in mixed kinetic/diffusive transport simulations which yield dynamic tension relaxations which are identical (to the experimental accuracy) to the diffusion-limited case; greater values for the kinetic constants are then large enough so that the kinetic transport is much faster than the diffusion process and the overall transport is diffusion limited. Note from table 2 how the value of the Biot number necessary for kinetics to be fast enough so that the drag coefficient (and hence the retardation) is diffusion limited is approximately ten times larger than the value necessary for the dynamic tension relaxation process to be diffusion limited. Thus the diffusive transport is faster in the case of bubble motion when compared to adsorption onto an initially clean interface, and this larger rate allows the observation of an effect of kinetics on the bubble motion and a resolution of the kinetic constants. These ideas are examined further in the related study Palaparthi *et al.* (2006).

We note finally from figure 13 that the interface remains completely stagnant as the concentration is increased from the critical value of $\approx 0.1\,\mathrm{mg\,l^{-1}}$ through C_{CMC} and up to $10 \times C_{CMC}$ (the highest concentration studied). For concentrations up to the CMC, this experimental result is consistent with the scaling arguments presented in the Introduction since at the CMC, $\chi(\exp K\Gamma_o/\Gamma_\infty + k)/Pe^{1/2} = 0.033$ and the bulk diffusion limitation alone can maintain the concentration gradient necessary to completely immobilize the surface. In addition, the exchange kinetics is slow; at the CMC, $Bi_{min}\{k + \exp(K\Gamma_o/\Gamma_\infty)\} \approx 0.05$. For concentrations above the CMC, the interface remains immobile as seen from figure 13. Above the CMC, micelles exchange with monomer in the bulk to maintain an equilibrium in which the bulk concentration is uniform and equal to the CMC. If the rate of this exchange is fast relative to convection and diffusion of the unaggregated surfactant, the sublayer concentration of monomer can become uniform, providing a remobilizing effect on the interfacial velocity as long as the surface kinetics is fast. For the case of this surfactant, the fact that the interface remains immobile above the CMC may be due to the relatively slow surface exchange kinetics which may offset the remobilization effect of the micellar exchange.

5. Conclusions

This study is a theoretical and experimental investigation of the effect of soluble surfactants on the motion of a bubble rising in a continuous liquid phase. We have examined the stagnant cap regime in which the rate of kinetic and diffusive transport of surfactant to the bubble interface is much slower than the rate at which surfactant is convected along the surface. Under these conditions and when surface diffusion is negligible, adsorbed surfactant is convected to a well-defined cap at the trailing edge of the rising bubble, while the front end remains surfactant-free.

Simulations were undertaken for spherical bubbles rising with order-one Reynolds numbers. The surfactant transport includes both finite kinetic exchange between the sublayer and the surface and diffusive and convective transport in the continuous phase at high Péclet numbers. We calculated the stagnant cap angle and corresponding flow and drag coefficient, as a function of the bulk concentration (for given surfactant transport parameters, Bi, Ma, χ, Pe). Our numerical results show that with the addition of even trace amounts of surfactant, the behaviour of the bubble changes from that with a completely stress-free interface to one with a completely stagnant interface, as seen by the change in the drag coefficient on the bubble. In addition, we demonstrate that for a fixed bulk concentration, the effect of kinetics is to reduce the cap angle, and hence the drag, relative to the diffusion-limited case.

Experiments were also undertaken to compare with the theoretical predictions. Terminal velocities of buoyantly rising bubbles in a 70:30 glycerol–water mixture were measured as a function of the bulk concentration of a polyethelene oxide surfactant ($C_{12}E_6$) dissolved in the continuous phase. Owing to the high viscosity of the mixture and the small size of bubles formed in our apparatus (about 0.3–0.8 mm in radius), bubble velocities are small enough to make the Weber and capillary numbers of order 10^{-2}; the bubble, therefore, experiences negligible distortion as we confirmed visually. The Reynolds numbers are approximately equal to 1 in the experiments. We measured the rise velocity, taking precautions that the bubbles were at steady state, as a function of bulk concentration. Our results show drag measurements of rising bubbles which are intermediate between a completely clean interface and a completely immobile one (i.e. stagnant caps with angles between 0 and 180°). The data show an increase in drag with bulk concentration and confirm the theoretical prediction that only a small bulk concentration is necessary to produce a completely immobile surface. To compare the data with the simulations we first measured independently the adsorption characteristics and diffusion coefficient of the surfactant for the glycerol–water mixture, using dynamic surface tension measurements obtained by the pendant bubble method. The dynamic tension experiments provide only a lower bound on the values of the kinetic coefficients α and β. We compared the measured drag coefficients to simulations at a low concentration at which the interface is partially immobilized, and found that the kinetic constants lie between the minimum value established by the dynamic tension measurements, and one an order of magnitude higher. This result suggests the possibility of using experiments involving the measurement of the drag on a bubble rising in a surfactant solution in the stagnant cap regime to measure the kinetic rate constants of a surfactant.

The work of C.M. was supported by NASA Grant NAG32167 and NAG32720. The work of D.T.P. was supported by NSF Grants DMS-0072228 and DMS-9872008.

Appendix. Numerical method of solution

In this Appendix we describe our numerical methods and the algorithm used to obtain steady solutions to our model. As we are particularly interested in obtaining results that can be compared directly with our experiments, the code described below is capable of producing results at high Péclet numbers and order-one Reynolds numbers.

A.1. *Spatial approximations and time advancement*

A finite volume method is employed to discretize the unsteady Navier–Stokes equations and the bulk surfactant transport equations (2.1)–(2.3). The momentum equations are solved in primitive variables, that is velocity and pressure variables. A staggered mesh, as shown in figure 14 is employed. The location of the nodes for the different variables is chosen as follows. The nodes for the concentration field C in the radial direction start at the bubble surface ($r=1$) and end at the outer edge of the numerical domain ($r=r_\infty$), while the nodes in the θ-direction start at $\theta=0$ and end at $\theta=\pi$. The nodes for the surface concentration Γ coincide with those of C on the bubble surface. The nodes for the radial velocity component u, follow the nodes for C but are staggered in the θ-direction so that a u-node is placed midway between neighbouring C nodes at a given radial position. It follows, then, that there are no u-nodes on the symmetry axes $\theta=0$ and $\theta=\pi$. The radial locations for the v-nodes are staggered relative to the C-nodes so that they are located midway between two

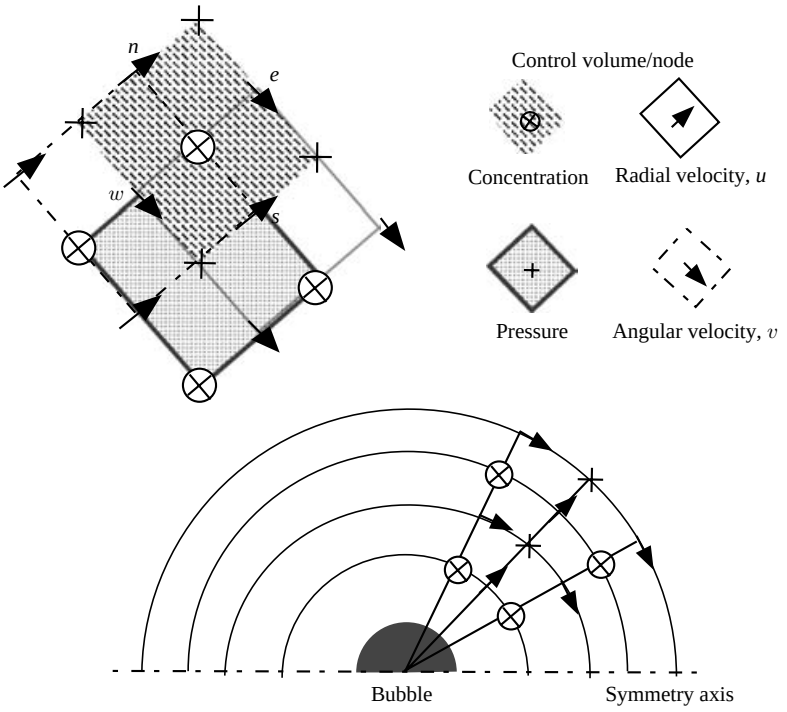

FIGURE 14. Typical staggered mesh for the finite volume method. ⊗ Concentration node; ↘ v-node; ↗ u-node; + pressure node.

C-nodes. Hence, the first v-node is located just below the surface of the bubble ($r < 1$ – this is a fictitious point), and the last v-node is positioned at $r < r_\infty$ midway between the last and second to last C-nodes. In the θ-direction the v-nodes are positioned at the same azimuthal locations as the C-nodes. Hence, they start from $\theta = 0$ and end at $\theta = \pi$. The control volumes for each of these variables are identified such that the node for that variable is placed at the centre of the control volume. This is shown in the top part of figure 14. The nodes for the pressure are located midway between those for u and v as shown in figure 14 (note that the first pressure node is off the bubble surface). In the top part of figure 14, the west side could represent the bubble surface.

The discretization of the momentum and concentration equations is achieved as follows. The radial and azimuthal components of the Navier–Stokes equations (2.1), are written in forms which facilitate a finite volume implementation, and which treat the convective and part of the viscous terms semi-implicitly in order obtain linear equations, as shown below:

$$\frac{\partial u}{\partial t} + \nabla\cdot\left(u\boldsymbol{v}^n - \frac{1}{Re}\nabla u\right) + \frac{1}{Re}\frac{\partial P}{\partial r} - \frac{(v^n)^2}{r} + \frac{2}{r^2 Re}\left(u^n + \frac{\partial v^n}{\partial\theta} + v^n\cot\theta\right) = 0, \quad \text{(A 1)}$$

$$\frac{\partial v}{\partial t} + \nabla\cdot\left(v\boldsymbol{v}^n - \frac{1}{Re}\nabla v\right) + \frac{1}{rRe}\frac{\partial P}{\partial\theta} + \frac{u^n v^n}{r} + \frac{2}{r^2 Re}\left(\frac{v^n}{2\sin^2\theta} - \frac{\partial u^n}{\partial\theta}\right) = 0, \quad \text{(A 2)}$$

The surfactant concentration equation becomes (treating convective terms explicitly)

$$\frac{\partial C}{\partial t} + \nabla\cdot\left(C\boldsymbol{v}^n - \frac{1}{Pe}\nabla C\right) = 0. \quad \text{(A 3)}$$

In the above $\boldsymbol{v}^n = u^n\boldsymbol{e}_r + v^n\boldsymbol{e}_\theta$ is the velocity field evaluated at the previous time step.

The concentration field equation (A 3) is integrated over its control volume and discretized in time over a time-step Δt. The result is

$$\frac{C^{n+1}-C^n}{\Delta t}\Delta V+\left(C^{n+1}u^n-\frac{1}{Pe}\frac{\partial C^{n+1}}{\partial r}\right)_e \mathrm{d}A_e-\left(C^{n+1}u^n-\frac{1}{Pe}\frac{\partial C^{n+1}}{\partial r}\right)_w \mathrm{d}A_w$$
$$-\left(C^{n+1}v^n-\frac{1}{rPe}\frac{\partial C^{n+1}}{\partial \theta}\right)_n \mathrm{d}A_n+\left(C^{n+1}v^n-\frac{1}{rPe}\frac{\partial C^{n+1}}{\partial \theta}\right)_s \mathrm{d}A_s=0. \quad (A\,4)$$

In the first term C denotes the value at the center of the cell. Here dA_i is the area of face i, where i = east, west, north, south of the control element of volume dV. In discretizing the area terms (without upwinding) which contain C and either $\partial C/\partial r$ or $\partial C/\partial\theta$, values of C from immediately adjacent cells are used. For the velocities at time level n, an average from the four u- or v-nodes surrounding the midpoint of the particular surface, is taken (see Griebel, Dornseifer & Neunhoeffer 1998). Because of the large values of the Péclet number we found it beneficial to use a hybrid upwinding scheme to evaluate derivatives of cell faces, as described by Patankar (1980). To complete the discretization, boundary conditions are adjoined to the control volumes adjacent to boundaries. Along the surface of the bubble, the balance of diffusive and kinetic fluxes is applied, with the surface concentration determined from the mass balance. Their incorporation is described in more detail in § A.3. Along the symmetry axis we have

$$\frac{\partial C}{\partial \theta}=0, \quad \theta=0,\pi \text{ (symmetry)}. \quad (A\,5)$$

Along the outer boundary of the computational domain, since the convection term dominates, the surfactant condition (2.10) at infinity is not applied directly but implemented in a different way in which different conditions are used at the inlet and outlet (see figure 2):

$$C=1, \quad 0<\theta<\pi/2 \text{ (inlet)}, \quad (A\,6)$$
$$\frac{\partial C}{\partial z}=0, \quad \pi/2<\theta<\pi \text{ (outlet)}. \quad (A\,7)$$

The outflow conditions on C are used in order to accurately model the solute wake that is present in the vicinity of the downstream axis of symmetry, at high Péclet numbers. Such boundary conditions have been used successfully in the related thermocapillary migration problem, at high Marangoni numbers, by Balasubramaniam & Lavery (1989) and Ma, Balasubramanian & Subramanian (1999).

For the solution of either (A 1) or (A 2) a projection method (see Chorin 1968) is used as described next. Time advancement by Δt from level n to $n+1$ is achieved in two steps: In the first half-step, the momentum equations are considered without the pressure gradient terms and integrations over corresponding control volumes are carried out. For (A 1) and (A 2) we write

$$\frac{u^*-u^n}{\Delta t/2}+\nabla\cdot\left(u^*\boldsymbol{v}^n-\frac{1}{Re}\nabla u^*\right)-\frac{(v^n)^2}{r}+\frac{2}{r^2Re}\left(u^n+\frac{\partial v^n}{\partial\theta}+v^n\cot\theta\right)=0, \quad (A\,8)$$
$$\frac{v^*-v^n}{\Delta t/2}+\nabla\cdot\left(v^*\boldsymbol{v}^n-\frac{1}{Re}\nabla v^*\right)+\frac{u^nv^n}{r}+\frac{2}{r^2Re}\left(\frac{v^n}{2\sin^2\theta}-\frac{\partial u^n}{\partial\theta}\right)=0, \quad (A\,9)$$

where (u^*, v^*) is the first approximation to the solution. The construction of the various terms over the bounding faces of a given cell is carried out using the averages and upwinding schemes described above. The boundary conditions necessary to complete the discretization are the zero normal velocity and tangential stress conditions on

the surface of the bubble (which are described in more detail in § A.3), symmetry conditions on the z-axis and the matching to the free-stream velocity (2.9) at the end of the computational domain r_∞. The matching at the outer boundary is done directly. Implementation of the stress boundary condition at the bubble surface requires the calculation of a radial derivative; owing to the way the θ-component of the velocity, v, is situated this necessitates the location of the fictitious point on the inside of the bubble surface as we mentioned earlier.

In the usual application of the method (see references above), all the convective and viscous terms are treated explicitly making it unnecessary to specify boundary conditions on u^* and v^* on the bubble surface, on the symmetry lines and at the bounding surface at infinity. We have constructed a semi-implicit time discretization that enables stability for larger time steps (see Peyret & Taylor 1983, for example). The terms treated semi-implicitly are those which are easily cast into conservative form so that their numerical evaluation by the volume of fluid method is straightforward. Owing to this method, boundary conditions are needed for u^* and v^*, and we take these to be the physical boundary conditions. We also note that the choice $u^* = 0$ on the boundary is consistent with that for the solution of the pressure Poisson equation, where it is used to obtain a unique solution (to within an arbitrary constant) for the pressure – see below for details.

In the second half-step only the pressure gradient contributions of (A 1) and (A 2) are considered in the time discretization. The pressure P^{n+1} at time level $n+1$ is calculated from the fact that the velocity $\boldsymbol{v}^{n+1}$ is divergence free:

$$\frac{\boldsymbol{v}^{n+1} - \boldsymbol{v}^*}{\Delta t/2} + \frac{1}{Re}\nabla P^{n+1} = 0, \tag{A 10}$$

$$\nabla \cdot \boldsymbol{v}^{n+1} = 0 \;\Rightarrow\; \nabla^2 P^{n+1} = \frac{2Re}{\Delta t}\nabla \cdot \boldsymbol{v}^*. \tag{A 11}$$

Note that the method is consistent as $\Delta t \to 0$.

In the Poisson equation (A 11) for the pressure, the right-hand side is known from the previous step. Integrating (A 11) over a pressure cell (see top part of figure 14) results in the following equation:

$$\left(\frac{\partial P}{\partial r}\right)_e \mathrm{d}A_e - \left(\frac{\partial P}{\partial r}\right)_w \mathrm{d}A_w - \left(\frac{1}{r}\frac{\partial P}{\partial \theta}\right)_n \mathrm{d}A_n + \left(\frac{1}{r}\frac{\partial P}{\partial \theta}\right)_s \mathrm{d}A_s = \frac{2Re}{\Delta t}(u_e^* dA_e - u_w^* dA_w - v_n^* dA_n + v_s^* dA_s) \tag{A 12}$$

To evaluate the pressure gradient $\partial P/\partial r$, say, on the east face of the pressure cell, the values of P at the P-nodes on the east and west sides of the cell are used. The fluxes on the right-hand side of (A 12) are easily evaluated since the normal velocity on each face is known because of the staggering (see figure 14). A key step in the implementation of (A 12) is the specification of a boundary condition for the pressure on the west side of the first box, i.e. on the bubble surface. This is discussed in detail in Griebel *et al.* (1998), and in what follows we give a brief outline specific to our calculation. In general $\partial P/\partial r$ is given by the radial component of equation (A 10); by substituting this into (A 12) we note that u^* at the bubble surface cancels out of the equation, indicating that u^* on the bubble surface can be arbitrarily chosen. This can also be done at the outer bounding surface of the computational domain. We choose $u^* = u^{n+1}$ to make $\partial P/\partial r = 0$ on the bubble surface and at the outer bounding surface, where we note that matching with the free-stream values provides the boundary condition $u^{n+1} = -\cos\theta$. On the symmetry lines $\theta = 0, \pi$, we

have $\partial P/\partial\theta = 0$, also. Our Poisson equation (A 11), then, is to be solved subject to the Neumann boundary condition $\boldsymbol{n}\cdot\nabla P^{n+1} = 0$, where $\boldsymbol{n}$ is the outward pointing normal to the computational domain. A solution will exist (to within an additive constant) as long as the compatibility condition is satisfied

$$\int_C \boldsymbol{n}\cdot\nabla P^{n+1}\mathrm{d}s = \int\int_D \frac{2Re}{\Delta t}\nabla\cdot\boldsymbol{v}^*\,\mathrm{d}\boldsymbol{x}. \tag{A 13}$$

The right-hand side is proportional to the line integral $\int_C \boldsymbol{n}\cdot\boldsymbol{v}^{n+1}\,\mathrm{d}s$ which is seen to be zero since $u^{n+1} = 0$ on the bubble surface and the symmetry lines, and $u^{n+1} = -\cos\theta$ at the outer boundary yielding a zero contribution there also. These observations and the existence of a solution to the Poisson equation result from the incompressibility of the flow $\boldsymbol{v}^{n+1}$.

Numerical solutions for u, v and C are updated over a time step by employing the ADI scheme (Alternating Directions Implicit Method). For example, u^* and v^* are calculated from time level n to level $n+1$ by using the ADI method, resulting in tridiagonal solvers (details can be found in Peyret & Taylor 1983, for example). At a given time level, the Poisson equation for the pressure P^{n+1} must be solved and this is achieved by employing a sparse matrix solver using the conjugate gradient method. Such schemes are highly efficient and this accelerated the computation times signifiantly. Once the solution P^{n+1} is found, the velocity field $\boldsymbol{v}^{n+1}$ follows from the identity (A 10). The steady state is assumed to be reached once the variation in quantities like u, v, C, is less than 0.01 % when measured 50 time steps apart.

A.2. *Grid construction*

Directly creating a grid on the physical domain (r, θ) requires an expanding mesh. We therefore use a grid based on a (x, y) coordinate system which transforms the physical domain into a rectangular domain through the logarithmic transformation $x = \ln(r)$ and the linear transformation $y = \theta/\pi$. Grid spacing is then set-up with even divisions in Δx and Δy. The magnitudes of the dimensionless groups are chosen to correspond with those of our experiments, so that we may model these experimental results. These are given in table 1. We note, however, that the Reynolds number, Re is of order one, and the Péclet number, Pe is of order 10^6. At such moderate values of the Reynolds number there are no significant boundary layer effects that would require more points near the surface, and in fact we found that the clustering inherent in the logarithmic transformation provides sufficient accuracy in computing the fluid dynamics. To avoid any artificial confinement of the flow by the outer boundary, the outer limit of the grid is fixed to correspond to r_∞ which is as large as 80 bubble radii. A 50×50 regular grid in (x, y) is used for the fluid dynamics in all the simulations reported here, unless otherwise stated.

Considering the transport of the surfactant from the bulk to the interface, the convective terms are dominant since the Péclet numbers are large (of order 10^6). For a fluid–fluid interface, at large Péclet numbers, there are steep gradients in the surfactant concentration field inside a boundary layer near the bubble surface. The thickness of this concentration boundary layer scales as $Pe^{-1/2}$ (Acrivos & Goddard 1965), and so a finer mesh is required near the bubble surface. To account for these large concentration gradients, we construct a hybrid grid to discretize the surfactant convection–diffusion equation. This grid is linear in r, extending from the surface of the bubble to a distance of order $Pe^{-1/2}$ and contains ten grid points. The edge of this inner mesh is made to coincide with the first radial grid line of the exponential coarse grid used for the fluid mechanics. Interpolated velocities at the concentration nodes are used in the solution of the concentration problem. We used a cubic spline

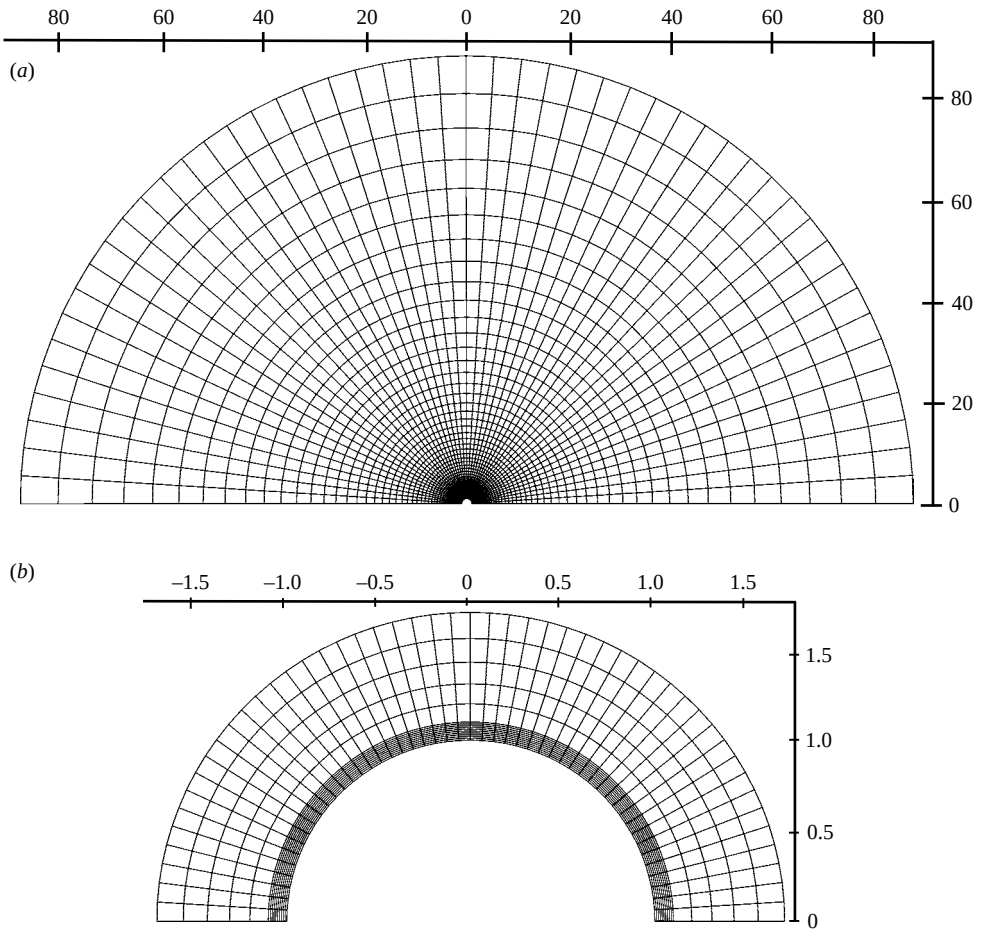

FIGURE 15. Numerical grid. (*a*) General view, (*b*) refinement near the bubble surface to numerically resolve the concentration boundary layer.

interpolation for this purpose. In addition, due to the smallness of the solute boundary layer, the numerical solution for the concentration can be confined to a smaller outer radius. We found from numerical experiments designed to validate the code (see below), that this outer boundary can be confined to about five bubble radii, with a coarser exponential grid of 100×100 and a fine inner mesh of 10×100. Figure 15(*a*) shows an example of an exponential grid for the velocity and in 15(*b*) the enlarged view of the finer mesh near the surface of the bubble used for the surfactant bulk concentration.

A.3. *Algorithm for the numerical solution*

The algorithm used to obtain the drag exerted on a rising bubble as a function of the surfactant bulk concentration is as follows.

(*a*) For given values of the cap angle ϕ and Reynolds number Re, the hydrodynamic flow around a spherical bubble with a solid cap of this size is solved using the time advancement as described above until steady state is reached. This is done using the mixed boundary conditions on the bubble surface of zero shear stress or zero tangential velocity (equations (2.14) and (2.16)), zero normal velocity on the bubble surface and matching to the far-field uniform flow (2.9). These conditions entirely

prescribe the flow in terms of the fixed Reynolds number Re. The shear stress on the bubble surface ($\tau_s(\theta;\phi)$, see equation (2.16)) is calculated at the surface concentration nodes and stored. In the evaluation of the drag, from equation (2.11), we need to know the pressure at the bubble surface. Since there is no pressure node on the bubble surface in the staggered grid used in the algorithm, pressure values are calculated using a three-point polynomial extrapolation. Normal stresses (τ_{rr}) which are only known at pressure nodes, are also extrapolated on the surface using the same procedure.

(b) Once the shear stress distribution on the solid part of the cap is computed, the surface concentration $\Gamma(\theta;\phi)$ on the cap is obtained from the tangential stress balance equation (2.17) for given values of Ma and K. This involves a numerical integration of the shear stress followed by a root-finder to calculate the surface concentration at a given node.

(c) Using the calculated surfactant surface concentration distribution on the cap region, the surfactant distribution in the continuous phase is calculated. This needs a value of the surfactant bulk concentration k. To start with, a value of k is guessed. When the kinetic exchange is fast ($Bi \gg 1$) the sublayer and surface are in equilibrium, and the dimensionless sublayer concentration can be calculated directly from the surface distribution as (see (2.18))

$$\left.\begin{aligned} C(1,\theta) &= \frac{1}{k}\left[\frac{\Gamma(\theta;\phi)\mathrm{e}^{K\Gamma(\theta;\phi)}}{1-\Gamma(\theta;\phi)}\right], \quad \pi-\phi<\theta<\pi, \\ C(1,\theta) &= 0 \quad 0<\theta<\pi-\phi \end{aligned}\right\}. \tag{A 14}$$

(d) With the sublayer concentration known and given a Péclet number, the distribution of surfactant in the continuous phase is obtained by solving the convection–diffusion equation with the velocity given by the hydrodynamic solution for the cap angle ϕ. The net flux to the bubble surface, given by the Nusselt number Nu (see equation (2.19)), is then computed from the surfactant distribution in the continuous phase. The first derivatives on the surface of the bubble required in estimating the net flux of surfactant to the bubble surface (as given by (2.19)), and which is needed to solve for the surfactant transport equation, are calculated using three-point formulas.

At steady state, the amount of surfactant adsorbing at the front end of the bubble, should balance the amount desorbing at the back end, hence implying that Nu is zero. In the results presented here, we assume convergence in k, if the absolute value of Nu is less than 0.1. This convergence criterion is due to the fact that at high Péclet numbers, Nu is of order $Pe^{1/3}$ to $Pe^{1/2}$ (the former estimate for a solid and the latter for a clean fluid interface). For our Péclet numbers, Nu is of order 10^2–10^3, unless k has the value satisfying the steady-state zero-flux condition. If the net flux is not converged to within this accuracy, the value of k is changed, and steps (c) to (d) are repeated, in an iterative manner, until Nu converges to its null steady-state value. Once convergence is reached, the cap angle and drag for particular values of k, Pe, Ma and K are known and noted. Steps (a) to (d) are repeated for different cap angles to get the drag as a function of k in the entire stagnant cap regime ($0<\phi<\pi$).

In situations where we have kinetic–diffusive transport (that is Bi is no longer asymptotically large), the quasi-equilibrium equations (A 14) are replaced by the balance between the kinetic and diffusive fluxes (equations (2.15) and (2.18)). The surfactant distribution in the continuous phase is then solved with the above two conditions, and the net flux to the surface is calculated as described previously in steps (a)–(d).

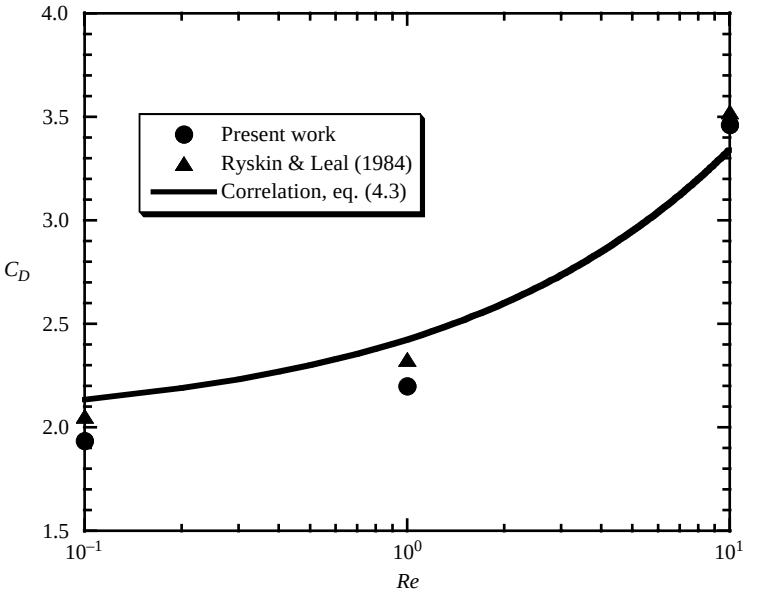

FIGURE 16. Drag coefficient on a spherical bubble as a function of Reynolds number. Comparison of the results of our simulations with those in previous studies.

Reynolds number *Re*	0	1	10	100
Drag coefficient on a spherical bubble				
Hadamard-Ribczynnski (1911)	2.00			
Ryskin & Leal (1982)		2.33	3.53	5.50
Present study	1.99	2.20	3.46	5.15
Drag coefficient on a solid sphere				
Stokes value	3.00			
Magnaudet *et al.* (1995)		3.72	6.52	19.13
Present study	3.12	3.67	6.46	19.29

TABLE 3. Drag coefficient on a spherical bubble and a solid sphere as a function of Reynolds number. Comparison of results from the present study and earlier works.

A.4. *Model validation*

As a first test, in figure 16, the drag coefficient C_D on a spherical bubble with a clean interface (the drag non-dimensionalized by the viscous scale $2\pi\mu a$) is calculated for different Reynolds numbers (0.1–10) and compared with the results of Ryskin & Leal's (1982) and the expression of Magnaudet *et al.* (1995) ($C_{D(Bubble)} = 2(1 + 0.21Re^{1/2})$) correlated from their numerical simulations and valid for *Re* less than 25. A further comparison of Ryskin & Leal's (1982) and our results at different $Re = 0$, 1, 10 and 10^2 is shown in table 3. Using a 50×50 grid with $r_\infty = 80$, the values of the drag predicted by the present simulation differ from those of the earlier works by about 5 % or less. We computed the drag on a solid sphere, with a no-slip boundary condition on the surface, to within approximately 1 % of those of previous work of Magnaudet *et al.* (1995) see also table 3.

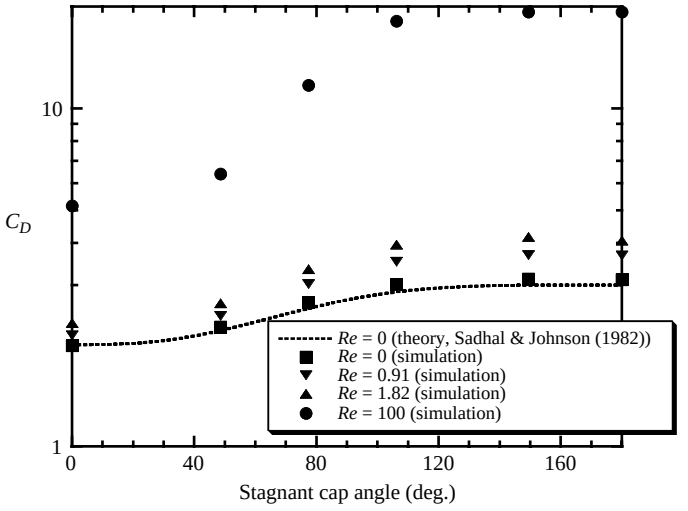

FIGURE 17. Drag coefficient against cap angle for $Re = 0$, 1.82 and 100.

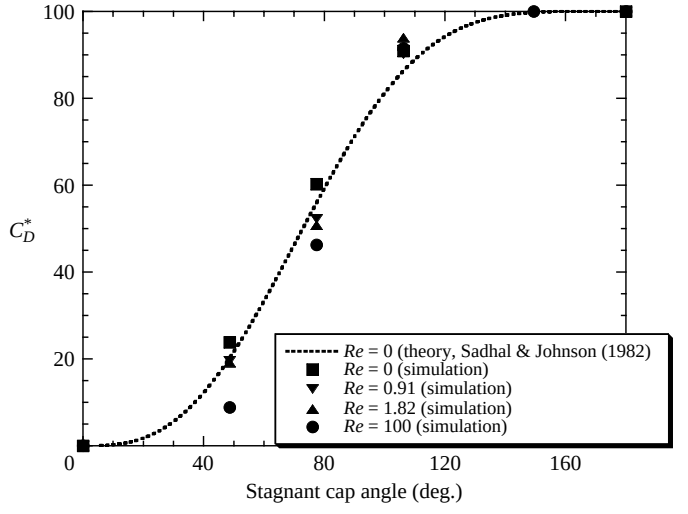

FIGURE 18. Scaled drag coefficient against cap angle for $Re = 0$, 1.82 and 100.

For the stagnant cap case, we compared the results of the present simulations at zero Reynolds number with the analytical solution given by Sadhal & Johnson (1982). With a 50×50 grid, we obtain drags, at different stagnant cap angles, to 5 % accuracy. These results are plotted for C_D, and a scaled drag coefficient C_D^*, the latter defined as

$$C_D^* = 100 \frac{\left[C_D - C_{D(Bubble)}\right]}{\left[C_{D(Solid)} - C_{D(Bubble)}\right]}, \tag{A 15}$$

against the cap angle, in figures 17 and 18 respectively. The quantities $C_{D(Bubble)}$ and $C_{D(Solid)}$ are the drags corresponding to a clean and solid interface respectively, and these are also obtained numerically using our code for non-zero Reynolds numbers. Also plotted are the results for order-one Reynolds number. We note that all the results exhibit similar features, indicating that the Reynolds number has a secondary

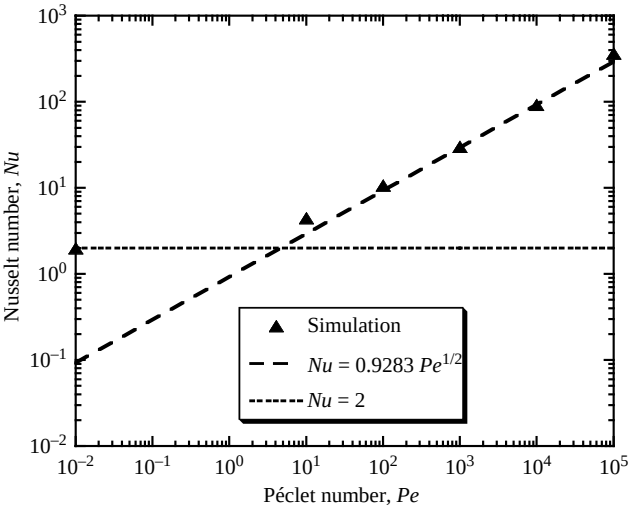

FIGURE 19. Verification of the code for surfactant bulk transport. Comparison of the results from our simulations with asymptotic and analytical solutions for the mass transfer rates (Nu) of a passive scalar to the bubble surface, for the case of a given creeping flow past the bubble when the bubble surface acts as a sink.

effect on the scaled drag coefficient. The main contribution to the drag on the bubble changes when the stagnant cap angle increases from around 50° to 110°. From figure 18, we note that with increasing Reynolds number, the drag coefficient increases more steeply with cap angle near the equator of the bubble, as also observed by others (Magnaudet *et al.* 1995; Takemura & Yabe 1999).

Solving the problem of the transport of a passive scalar in creeping flow conditions past a bubble with a stress-free interface, when the bubble acts as a sink, checks the code for the surfactant bulk transport equation. The Nusselt number defined by (2.19) gives the net scalar flux to the bubble surface. We found good agreement, for the Nusselt number, between our solution of the surfactant bulk transport problem with a given creeping flow and the asymptotic results of Acrivos & Goddard (1965) for the range of Péclet numbers of our interest (of orders 10^3–10^6) – see figure 19. Note that for the calculation shown in this figure, at zero and low Péclet numbers, we used a numerical domain extending to 80 bubble radii. But at higher Péclet numbers ($> 10^3$) a domain extending to 5 bubble radii is found to be sufficiently accurate with grids of size 110×100 (a 100×100 exponential grid coupled with a 10×100 linear grid spread within the solute boundary layer close to the surface of the bubble as explained earlier).

REFERENCES

ACRIVOS, A. & GODDARD, J. 1965 Asymptotic expansions for laminar forced convection heat and mass transfer. *J. Fluid Mech.* **23**, 273–291.

ANDREWS, G., FIKE, R. & WONG, S. 1988 Bubble hydrodynamics and mass transfer at high reynolds number and surfactant concentration. *Chem. Engng Sci.* **43**, 1467–1477.

BALASUBRAMANIAM, R. & LAVERY, J. 1989 Numerical solution of thermocapillary bubble migration under microgravity for large reynolds and marangoni numbers. *Numer. J. Heat Transfer* A **16**, 175–187.

Beitel, A. & Heideger, W. J. 1971 Surfactant effects on mass transfer from drops subject to interfacial instability. *Chem. Engng Sci.* **26**, 711–717.

Bel Fdhila, R. & Duineveld, P. C. 1996 The effect of surfactants on the rise of a spherical bubble at high reynolds and peclet numbers. *Phys. Fluids* **8**, 310–321.

Bond, W. & Newton, D. A. 1928 Bubbles, drops and Stokes' law. *Phil. Mag.* **5**, 794–800.

Borwankar, R. & Wasan, D. 1983 The kinetics of adsorption of surface active agents at gas-liquid surfaces. *Chem. Engng Sci.* **38**, 1637–1649.

Boye-Christensen, G. & Terjesen, S. G. 1958 On the mechanism of interfacial resistance to mass transfer in liquid-liquid extraction. *Chem. Engng Sci.* **7**, 222–229.

Boye-Christensen, G. & Terjesen, S. G. 1959 On the action of surface active agents on mass transfer in liquid liquid-extraction. *Chem. Engng Sci.* **9**, 225–241.

Chang, C. H. & Franses, E. 1995 Adsorption dynamics of surfactants at the air/water interface: a critical review of mathematical models, data, and mechanisms. *Colloids Surfaces* **100**, 1–45.

Chen, J. & Stebe, K. 1996 Marangoni retardation of the terminal velocity of a setting droplet: The role of surfactant physio-chemistry. *J. Colloid Interfacial Sci.* **178**, 144–155.

Chen, J. & Stebe, K. 1997 Surfactant-induced retardation of the thermocapillary migration of a droplet. *J. Fluid Mech.* **340**, 35–60.

Chorin, A. J. 1968 Numerical solution of navier-stokes equations. *Math. Comput.* **22**, 745–762.

Clift, R., Grace, J. & Weber, M. 1978 *Bubbles, Drops and Particles.* Academic.

Cuenot, B., Magnaudet, J. & Spennato, B. 1997 The effects of slightly soluble surfactants on the flow around a spherical bubble. *J. Fluid Mech.* **339**, 25–53.

Davis, R. E. & Acrivos, A. 1966 The influence of surfactants on the creeping motion of bubbles. *Engng Sci.* **21**, 681–685.

Deryagin, B., Dukhin, S. & Lisichenko, V. 1959 The kinetics of the attachment of mineral particles to bubbles during flotation. i. the electric field of a moving bubble. *Russ. J. Phys. Chem* **33**, 389–393.

Deryagin, B., Dukhin, S. & Lisichenko, V. 1960 The kinetics of the attachment of mineral particles to bubbles during flotation. ii. the electric field of a moving bubble when the surface activity of the iogenic substance is high. *Russ. J. Phys. Chem* **34**, 248–251.

Duineveld, P. 1995 The rise velocity and shape of bubbles in pure water at high reynolds number. *J. Fluid Mech.* **292**, 325–332.

Dukhin, S. & Buikov, M. 1965 Theory of the dynamic adsorption layer of moving spherical particles. ii. theory of the dynamic adsorption layer of a bubble (drop) at a reynolds number re¡¡1 in the prtesence of strong retardation of the surface. *Rus. J. Phys. Chem.* **39**, 482–485.

Edge, R. & Grant, C. 1972 The motion of drops in water contaminated with a surface active agent. *Chem. Engng Sci.* **27**, 1709–1721.

Edwards, D. A., Brenner, H. & Wasan, D. 1991 *Interfacial Transport Processes and Rheology*. Butterworth-Heinemann.

Elzinga, E. & Banchero, J. T. 1961 Some observations on the mechanics of drops in liquid-liquid systems. *AICHE J.* **7**, 394–399.

Frumkin, A. & Levich, V. 1947 Some factors affecting droplet behavior in liquid-liquid systems. *Zhur. Fiz. Khim.* **21**, 1183–1204.

Garner, F. & Haycock, P. 1959 The effect of surface active agents on extraction. *Proc. R. Soc. Lond.* A **252**, 457–463.

Garner, F. H. & Hale, A. 1953 The effect of surface active agents on liquid extraction processes. *Chem. Engng Sci.* **2**, 157–163.

Garner, F. H. & Skelland, H. 1955 Some factors affecting droplet behavior in liquid-liquid systems. *Chem. Engng Sci.* **17**, 1057–1070.

Griebel, M., Dornseifer, T. & Neunhoeffer, T. 1998 *Numerical Simulation in Fluid Dynamics. A Practical Introduction.* SIAM.

Griffith, R. 1962 The effect of surfactants on the terminal velocity of drops and bubbles. *Chem. Engng Sci.* **17**, 1057–1710.

Harper, J. 1972 The motion of bubbles and drops through liquids. *Adv. Appl. Mech.* **12**, 59–129.

Harper, J. 1973 On bubbles with small immobile adsorbed films rising in liquids at low reynolds numbers. *J. Fluid Mech.* **58**, 539–545.

Harper, J. 1974 On spherical bubbles rising steadily in dilute surfactant solutions. *Q. J. Mech. Appl. Maths* **27**, 87–100.

Harper, J. 1982 Surface activity and bubble motion application. *Appl. Sci. Res.* **38**, 343–351.

Harper, J. 1988 The rear stagnation region of a bubble rising steadily in a dilute surfactant solution. *Q. J. Mech. Appl. Maths* **41**.

Harper, J. F. 2004 Stagnant-cap bubbles with both diffusion and adsorption rate-determining. *J. Fluid Mech.* **521**, 115–123.

He, Z., Maldarelli, C. & Dagan, Z. 1991 The size of stagnant caps of bulk soluble surfactant on the interfaces of translating fluid droplets. *J. Colloid Interfacial Sci.* **146**, 442–451.

Holbrook, J. A. & Levan, M. D. 1983*a* Retardation of droplet motion by surfactant. part ii. numerical solutions for exterior diffusion, surface diffusion, and adsorption kinetics. *Chem. Engng Commun.* **20**, 273–290.

Holbrook, J. A. & Levan, M. D. 1983*b* Retardation of droplet motion by surfactant. part i. theoretical development and asymptotic solutions. *Chem. Engng Commun.* **20**, 191–207.

Holm, A. & Terjesen, S. 1955 The effect of a surface active agent on mass transfer in a liquid-liquid extractor. *Chem. Engng Sci.* **4**, 265–268.

Horton, T. J., Fritsch, T. R. & Kintner, R. C. 1965 Experimental determination of circulation velocities inside drops. *Can. J. Chem. Engng* **43**, 143–146.

Huang, W. S. & Kintner, R. C. 1969 Effects of surfactants on mass transfer inside drops. *AICHE J.* **15**, 735–744.

Jachimska, B., Warszynski, P. & Malysa, K. 2001 Influence of adsorption kinetics and bubble motion on stability of the foam films formed at n-octanol, n-hexanol and n-butonal solution surface. *Colloids Surfaces* A **192**, 177–193.

Kim, H. & Subramanian, R. 1989 Thermocapillary migration of a droplet with insouble surfactant, i. surfactant cap. *J. Colloid Interface Sci.* **127**, 417–430.

Krzan, M. & Malysa, K. 2002 Profiles of local velocities of bubbles in n-butonol, n-hexanol and n-nonanol solutions. *Colloids Surfaces* A **207**, 279–291.

Leppinen, D. M., Renksizbulut, M. & Haywood, R. J. 1996*a* The effects of surfactants on droplet behaviour at intermediate reynolds numbers- i. the numerical model and steady-state results. *Chem. Engng Sci.* **51**, 479–489.

Leppinen, D. M., Renksizbulut, M. & Haywood, R. J. 1996*b* The effects of surfactants on droplet behaviour at intermediate reynolds numbers-ii. transient deformation and evaporation. *Chem. Engng Sci.* **51**, 491–501.

Levan, M. & Newman, J. 1976 The effect of surfactant on the terminal and interfacial velocities of a bubble or drop. *AICHE J.* **22**, 695–701.

Levich, V. 1962 *Physicochemical Hydrodynamics*. Prentice Hall.

Liao, Y. & McLaughlin, J. 2000*a* Bubble motion in aqueous surfactant solutions. *J. Colloid Interface Sci.* **224**, 297–310.

Liao, Y. & McLaughlin, J. 2000*b* Dissolution of a freely rising bubble in aqueous surfactant solutions. *Chem. Engng Sci.* **55**, 5831–5850.

Liao, Y., Wang, J., Nunge, R. & McLaughlin, J. 2004 Comments on "bubble motion in aqueous surfactant solutions". *J. Colloid Interface Sci.* **272** (2), 498–501.

Lindland, K. & Terjesen, S. 1956 The effect of surface active agents on liquid-liquid mass transfer rates. *Chem. Engng Sci.* **5**, 1–16.

Ma, X., Balasubramanian, R. & Subramanian, R. 1999 Numerical simulation of thermocapillary drop motion with internal circulation. *Numer. Heat Transfer* A **35**, 291–309.

Magnaudet, J., Rivero, M. & Fabre, J. 1995 Accelerated flows past a rigid sphere or a spherical bubble. part 1. steady straining flow. *J. Fluid Mech.* **284**, 97–135.

Maxworthy, T., Gnann, C., Kurten, M. & Durst, F. 1996 Experiments on the rise velocity of air bubbles in clean viscous liquiids. *J. Fluid Mech.* **321**, 421–441.

McLaughlin, J. B. 1996 Numerical simulation of bubble motion in water. *J. Colloid Interface Sci.* **184**, 613–625.

Mekasut, L., Molinier, J. & Angelino, H. 1978 Effects of surfactants on mass transfer outside drops. *Chem. Engng Sci.* **33**, 821–829.

Palaparthi, R., Papageorgiou, D. & Maldarelli, C. 2006 Determination of the kinetic rate constants for surfactant adsorption by measurement of the velocities of rising bubles with stagnant surfactant caps. *J. Colloid Interface Sci.* (to be submitted).

Patankar, S. V. 1980 *Numerical Heat Transfer and Fluid Flow*. Hemisphere.

Peyret, R. & Taylor, T. D. 1983 *Computatioal Methods for Fluid Flow*. Springer.

Ponoth, S. & McLaughlin, J. 2000 Numerical simulation of mass transfer for bubbles in water. *Chem. Engng Sci.* **55**, 1237–1255.

Raymond, D. & Zieminski, S. 1971 Mass transfer and drag coefficients of bubbles rising in dilute aqueous solutions. *AICHhE J* **17**, 57–65.

Ryskin, G. & Leal, L. G. 1982 Numerical solution of free-boundary problems in fluid mechanics. *J. Fluid Mech.* **148**, 1–17.

Sadhal, S. & Johnson, R. 1982 Stokes flow past bubbles and drops partially coated within films. part 1. stagnant cap of surfactant film-exact solution. *J. Fluid Mech.* **126**, 237–250.

Sam, A., Gomez, C. & Finch, J. 1996 Axial velocity profiles of single bubbles in water/frother solutions. *Intl J. Mineral Processes* **47**, 177–196.

Savic, P. 1953 Circulation and distortion of liquid drops falling through a viscous medium. *Natl Res. Counc. Can. Div. Mech. Engng Rep.* MT-22.

Saville, D. 1973 The effects of interfacial tension on the motion of drops and bubbles. *Chem. Engng J.* **5**, 251–259.

Skelland, A. & Huang, Y.-F. 1977 Effects of surface active agents on fall velocities of drops. *Can. J. Chem. Engng* **55**, 240245.

Skelland, A., Woo, S. & Ramsay, G. 1987 Effect of surface active agents on drop size, terminal velocity and droplet oscillation in liquid-liquid systems. *Ind. Engng Chem. Res.* **26**, 907–911.

Suzin, Y. & Ross, S. 1985 Retardation of the ascent of gas bubbles by surface-active solutes in nonaqueous solutions. *J. Colloid Interface Sci.* **103**, 578–585.

Takemura, F. 2005 Adsorption of surfactants onto the surface of a spherical rising bubble and its effect on the terminal velocity of the bubble. *Phys. Fluids* **17**, 048104–048114.

Takemura, F. & Yabe, A. 1999 Rising speed and dissolution rate of a carbon dioxide bubble in slightly contaminated water. *J. Fluid Mech.* **378**, 319–334.

Wang, Y., Papageorgiou, D. & Maldarelli, C. 1999 Increased mobility of a surfactant retarded bubble at high bulk concentrations. *J. Fluid Mech.* **390**, 251–270.

Wang, Y., Papageorgiou, D. & Maldarelli, C. 2001 Using surfactants to control the formation and size of wakes behind moving bubbles at order one reynolds numbers. *J. Fluid Mech.* **453**, 1–19.

Yamamoto, T. & Ishil, T. 1987 Effect of surface active materials on the drag coefficients and shapes of single large gas bubbles. *Chem. Engng Sci.* **42**, 1297–1303.

Ybert, C. & Meglio, J. D. 2000 Ascending air bubbles in solutions of surface active molecules: influence of desorption kinetics. *Eur. Phys. J.* E **3**, 143–148.

Zhang, Y. & Finch, J. 2001 A note on single bubble motion in surfactant solutions. *J. Fluid Mech.* **429**, 63–66.

Zhang, Y., McLaughlin, J. & Finch, J. 2001 Bubble velocity profile and model of surfactant mass transfer to bubble surface. *Chem. Engng Sci.* **56**, 6605–6616.

Zhang, Y., Sam, A. & Finch, J. 2003 Temperature effect on single bubble velocity profile in water and surfactant solution. *Colloids Surfaces* A **223**, 45–54.